HHS Public Access

Author manuscript

Neurobiol Aging. Author manuscript; available in PMC 2022 February 01.

Published in final edited form as:

Neurobiol Aging. 2021 February ; 98: 63–77. doi:10.1016/j.neurobiolaging.2020.09.018.

Modulation of OSCP mitigates mitochondrial and synaptic deficits in a mouse model of Alzheimer's pathology

Esha Gauba[1,#], **Shaomei Sui**[1,#], **Jing Tian**[1], **Christopher Driskill**[2], **Kun Jia**[1], **Chunxiao Yu**[1], **Tripta Rughwani**[1], **Qi Wang**[1], **Sven Kroener**[2], **Lan Guo**[1,*], **Heng Du**[1,*]

[1]Department of Biological Sciences, University of Texas at Dallas. Richardson, TX, 75080

[2]School of Behavioral and Brain Sciences, University of Texas at Dallas. Richardson, TX, 75080

Abstract

Synaptic failure underlies cognitive impairment in Alzheimer's disease (AD). Cumulative evidence suggests a strong link between mitochondrial dysfunction and synaptic deficits in AD. We previously found that oligomycin-sensitivity conferring protein (OSCP) dysfunction produces pronounced neuronal mitochondrial defects in AD brains and a mouse model of AD pathology (5xFAD mice). Here, we prevented OSCP dysfunction by overexpressing OSCP in 5xFAD mouse neurons in vivo (Thy-1 OSCP/5xFAD mice). This approach protected OSCP expression and reduced interaction of amyloid beta (Aβ) with membrane-bound OSCP. OSCP overexpression also alleviated F1Fo ATP synthase deregulation and preserved mitochondrial function. Moreover, OSCP modulation conferred resistance to Aβ-mediated defects in axonal mitochondrial dynamics and motility. Consistent with preserved neuronal mitochondrial function, OSCP overexpression ameliorated synaptic injury in 5xFAD mice as demonstrated by preserved synaptic density, reduced complement-dependent synapse elimination, and improved synaptic transmission, leading to preserved spatial learning and memory. Taken together, our findings show the consequences of OSCP dysfunction in the development of synaptic stress in AD-related conditions and implicate OSCP modulation as a potential therapeutic strategy.

[*]**Corresponding authors: Lan Guo** MD PhD, Assistant Research Professor, Department of Biological Sciences, The University of Texas at Dallas Richardson, TX, 75080, lan.guo@utdallas.edu, 9728833531, **Heng Du** MD PhD, Associate Professor, Department of Biological Sciences, The University of Texas at Dallas, Richardson, TX, 75080, Heng.du@utdallas.edu, 9728833532.

[#]Contribute equally

AUTHORS' CONTRIBUTIONS: EG, SS, JT, CD, CY, KJ, TR and QW performed experiments. LG and HD conceived the study. SK, LG and HD contributed to data interpretation and experimental design. HD wrote the manuscript. Tienju Wang helped with figure preparation and proofreading. All authors read and approved the final manuscript.

Credit Author Statement

Esha Gauba, Shaomei Sui, Jing Tian, Christopher Driskill, Chunxiao Yu, Kun Jia, Tripta Rughwani and Qi Wang performed experiments. Lan Guo and Heng Du conceived the study. Sven Kroener, Lan Guo and Heng Du contributed to data interpretation and experimental design. Heng Du wrote the manuscript. Tienju Wang helped with figure preparation and proofreading. All authors read and approved the final manuscript.

COMPETING INTERESTS

The authors have no conflict of interest to claim.

Keywords

Oligomycin sensitivity-conferring protein; mitochondrial F1Fo ATP synthase; synaptic injury; amyloid beta; Alzheimer's disease

1. INTRODUCTION

Alzheimer's disease (AD) is a chronic neurodegenerative disorder characterized by insidious onset and progressive cognitive decline (Querfurth and LaFerla, 2010). Effective treatments that benefit patients with AD are still lacking. Although amyloid beta (Aβ) deposition is a defining pathology of AD (Hardy and Higgins, 1992), recent clinical failures challenged the effectiveness of interventions against Aβ *per se* for the treatment of this neurological disorder (Honig et al., 2018; Selkoe, 2019), prompting a reappraisal of alternative therapeutic pathways. Previous observations of brain hypometabolism, oxidative damages, and energy deficiency support the mitochondrial cascade hypothesis of AD (Mosconi et al., 2008; Reddy, 2009; Swerdlow, 2018). Mitochondrial dysfunction and synaptic damage are early events in AD; however, the underlying mechanisms are unclear (Reddy et al., 2012; Swerdlow et al., 2014). For this reason, mitochondrial dysfunction that contributes to AD-related neuronal perturbations might provide novel therapeutic targets to prevent neurodegenerative processes that stem from Aβ toxicity.

Reduced energy production due to compromised oxidative phosphorylation (OXPHOS) is a prominent feature of mitochondrial pathology in AD neurons. In addition to defects in the mitochondrial electron transport chain (ETC), deregulation of F1Fo ATP synthase, the key enzyme for mitochondrial OXPHOS (Walker, 1998; Walker et al., 1987), has been linked to lowered OXPHOS efficacy in cognitive aging (Gauba et al., 2017) and AD (Beck et al., 2016; Gauba et al., 2019). Oligomycin sensitivity-conferring protein (OSCP), a component of the F1Fo ATP synthase peripheral stalk, is a critical subunit for the structural stability and function of this enzyme (Rubinstein et al., 2003; Wilkens and Capaldi, 1998). Patients with AD show loss of OSCP and OSCP/Aβ complexation in their brains (Beck et al., 2016). These OSCP abnormalities are believed to underlie F1Fo ATP synthase deregulation and they contribute to neuronal mitochondrial dysfunction in AD-relevant settings (Beck et al., 2016; Gauba et al., 2019; Gauba et al., 2017). Given the pivotal role of mitochondrial fitness in synaptic physiology (Du et al., 2010; Guo et al., 2017; Ly and Verstreken, 2006), the deleterious impact of OSCP changes on mitochondrial function implicates an OSCP-related mechanism of synaptic failure in AD. We therefore hypothesized that OSCP perturbations could be targeted to mitigate Aβ-induced synaptic stress.

To experimentally address this idea, we overexpressed OSCP in neurons under the control of the Thy-1 promoter in 5xFAD mice (Thy-1 OSCP/5xFAD mice). This modulation restored OSCP expression without affecting other major F1Fo ATP synthase subunits in 5xFAD mice. Moreover, the complexation of Aβ with inner mitochondrial membrane (IMM)-bound OSCP was attenuated by OSCP overexpression. In addition to its beneficial effect on F1Fo ATP synthase activity and mitochondrial bioenergetics in 5xFAD mice, OSCP overexpression prevented axonal mitochondrial dynamics and motility from Aβ toxicity.

Importantly, Thy-1 OSCP/5xFAD mice exhibited normal synaptic density and synaptic transmission, as well as reduced synapse pruning, and preserved cognitive performances. Our findings suggest a role of neuronal OSCP dysfunction in the pathogenesis of synaptic degeneration in AD-related pathological settings and suggest novel pathways in the development of treatments for AD.

2. METHODS AND MATERIALS

2.1 Mice.

Animal studies were approved and performed under the guidelines of the University of Texas at Dallas (UTD) Institutional Animal Care and Use Committee (IACUC) and National Institutes of Health (NIH). In order to generate Thy-1 OSCP transgenic mice, a recombinant vector was designed to place human OSCP cDNA (Gene Name: ATP5O. NCBI Gene ID: 539) under control of mouse *Thy1* gene promoter [gift from Joshua R. Sanes (Feng et al., 2000): Addgene plasmid 20736]. This construct was microinjected into pronuclei of single-cell B6SJLF1/J hybrid embryos by the staff at the transgenic core at UT Southwestern Medical Center. Founder transgenic mice were identified by PCR and confirmed by Southern blot analysis. Transgenic founders were backcrossed to B6SJLF1/J background.

Thy-1 OSCP mice were crossed with 5xFAD mice (B6SJL-Tg(APP-SwFlLon, PSEN1*M146L*L286V)6799Vas/Mmjax), which were originally obtained from Jackson Laboratory to generate litters including non-transgenic (nonTg), 5xFAD, Thy-1 OSCP, and Thy-1 OSCP/5xFAD mouse. Genotypes of animals were confirmed using PCR and/or amyloid plaque staining. The minimum number of mice needed was determined by power calculation based on our previous results. To mimic mild cognitive impairment (MCI) and later stage AD, respectively, the studies were performed using 4–5 and 9–10-month-old mice. Both male and female mice were used.

2.2 Immunoblotting.

Samples were prepared as previously described (Beck et al., 2016). Mitochondria samples were prepared and lysed in RIPA lysis buffer (50 mM Tris-HCl, pH 8.0, with 150 mM sodium chloride, 1.0% NP-40, 0.5% sodium deoxycholate, and 0.1% sodium dodecyl sulfate). Neurons were collected in sample loading buffer (50 mM Tris-HCl pH 6.8, 2% SDS, 10% glycerol, 1% β-mercaptoethanol, 12.5 mM EDTA and 0.02% bromophenol blue) with Protease Inhibitor Cocktail Set V (Millipore) and phosphatase inhibitors including Sodium Fluoride (Sigma-Aldrich) and Sodium Orthovanadate (Sigma-Aldrich). Proteins were separated on a 12% Bis-tris gel (NuPage, Life Technologies) and transferred to PVDF membrane (ImmunBlot membrane, BioRad) at 120V for 90 minutes. Membranes were blocked with 5% milk (Labscientific Inc) for 1 hour at room temperature followed by primary antibody incubation for overnight at 4 °C. The following day, membranes were washed with 1×TBS and incubated with secondary antibody at the appropriate concentration. The following antibodies were used in this study: anti-Aβ (CST, 1:1000), anti-Tom40 (Santa Cruz, 1:500), anti-a subunit (Proteintech, 1:5000), anti-b subunit (Santa Cruz, 1:500), anti-c subunit (Abcam, 1:3000), anti-OSCP (Santa Cruz, 1:5000), anti-α subunit (Santa Cruz, 1:5000), anti-β subunit (Santa Cruz, 1:5000), anti-γ subunit (Santa

Cruz, 1:5000), anti-Opa1 (BD Biosciences, 612606, 1:1000), anti-Mitofusin-2 (Mfn2) (Cell Signaling Technology, 9482S, 1:3000), anti-Dynamin Like Protein-1 (Dlp1) (BD Biosciences, 611112, 1:2000), anti-phospho-Dlp1 (Ser616) (Cell Signaling Technology, 3455), anti-C1q (Dako, A0136, 1:1000), rabbit monoclonal anti-MCU antibody (CST, 14997s, 1:4000), rabbit monoclonal anti-MICU1 antibody (CST, 12524, 1:1,000), rabbit polyclonal anti-MICU2 antibody (Abcam, ab101465, 1:1,000), rabbit polyclonal anti-MICU3 antibody (Invitrogen, PA5–55177, 1:1000), rabbit polyclonal anti-SMDT1 (EMRE) antibody (Sigma, HPA032117, 1:1,000), rabbit polyclonal anti-CCDC109B (Mcub) antibody (Proteintech, 20387–1-AP, 1:1,000), rabbit polyclonal anti-TOMM40 antibody (Proteintech, 18409–1-AP, 1:10,000), HRP conjugated goat anti-mouse IgG (H+L) (Thermo Fisher Scientific, 626520, 1:2000), and HRP conjugated goat anti-rabbit IgG (H+L) (Thermo Fisher Scientific, 656120, 1:2000). Images were collected on a Bio-Rad Chemidoc Imaging System. Image J (National Institutes of Health) was used to analyze the blots and to quantify protein signal intensity.

2.3 Synaptosome isolation.

Synaptosomes were isolated as previously described (Beck et al., 2016; Gauba et al., 2019). In brief, brain tissues were homogenized in ice cold buffer [225 mM mannitol, 75 mM sucrose, 2 mM K_2PO_4, 0.1% BSA, 5 mM Hepes, and 1 mM EGTA (pH 7.2)] using a Wheaton Dounce homogenizer. The resultant homogenate was centrifuged at 1,300 × g for 3 minutes to remove blood and cell debris in the pellet, and the supernatant was layered on a discontinuous Percoll density gradient consisting of 15%, 23%, and 40% (vol/ vol) Percoll. After centrifugation at 34,000 × g for 5 minutes, synaptosomes were collected from the interface between 15% and 23% Percoll.

2.4 Brain mitochondria isolation.

Brain mitochondria were prepared as previously described (Gauba et al., 2019). Cortices were dissected from mouse brain and homogenized in ice cold isolation buffer [225 mM mannitol, 75 mM sucrose, 2 mM K2PO4, 0.1% BSA, 5 mM Hepes, and 1 mM EGTA (pH 7.2)] with a Wheaton Dounce homogenizer. After a centrifugation at 1,300 × g for 5 minutes to remove blood and cell debris, the supernatant was layered on 15% Percoll (GE) and centrifuged at 12,500 × g for 10 minutes. The pellets were collected and resuspended in isolation buffer with 0.02% Digitonin (Sigma-Aldrich), followed by centrifugation at 8,000 × g for another 10 minutes. The pellets were then washed with an additional centrifugation step in ice-cold isolation buffer without EGTA for experiments. Protein concentrations were measured using Bradford assay for protein detection (BioRad).

2.5 Mitochondrial membrane isolation.

The isolated mitochondria were broken in isolation buffer containing 5% Digitonin on ice for 15 minutes followed by sonication on ice for 20 minutes. The mitochondrial membranes were pelleted by centrifugation at 130,000 × g for 1 hour at 4 °C using a Beckman Coulter ultracentrifuge (Optima XPN-90).

2.6 Co-immunoprecipitation (Co-IP) of OSCP and Aβ.

Co-immunoprecipitation was performed using 0.5 mg of mitochondria or mitochondrial membrane-rich fractions. The indicated fractions were lysed using Lysis buffer (50 mM Tris-HCl, 150 mM NaCl, 1 mM EDTA, 0.5% NP-40, 5% glycerol and 1X protease inhibitor) by incubation on ice for 30 minutes, then subjected to five freeze-thaw cycles, followed by centrifugation at 12,500 × g for 10 minutes at 4 °C. The Supernatants were incubated with anti-OSCP (Santa Cruz, 0.5 μg IgG/100 μg protein) to form immune-complexes at 4 °C overnight. Pre-immune IgG was used at the same concentration to determine protein-protein interaction specificity. The immune-complexes were precipitated by using pre-cleaned A/G beads (Pierce), followed by immunoblotting with antibody to Aβ (CST, 1:1000) to identify OSCP-Aβ interaction.

2.7 Duolink proximity ligation assay (PLA).

The interaction between OSCP and Aβ in mouse brain slices was detected using Duolink In Situ PLA detection kits (Sigma-Aldrich) following the manufacturer's instruction. Mouse anti-OSCP (Santa Cruz Biotechnologies, 1: 200) and rabbit anti-Aβ (CST, 1:1000) were used as primary antibodies. Anti-Rabbit PLUS (Sigma-Aldrich, #DUO92002) and anti-Mouse MINUS (Sigma-Aldrich, #DUO92004) were applied as Duolink in Situ PLA Probes. Images were collected on a Nikon confocal microscope. The images were converted to three dimensional images by using the Nikon NIS Elements Advanced Research Software "3D reconstruction" module for analysis. The number of PLA-positive dots was counted, and divided by total volume of the image stack.

2.8 F1FO ATP synthase enzymatic activity assay.

F1FO ATP synthase enzyme activity was measured spectrophotometrically using NADH-linked ATP regenerating system. Mitochondria were resuspended in activity assay buffer [100 mM Tris HCl (pH 7.4), 2 mM MgCl2, 50 mM KCl, 0.2 mM EDTA, 0.23 mM NADH, and 1 mM phosphoenolpyruvate). The reaction was triggered by adding 0.4 M Mg-ATP and recorded on a spectrophotometer at OD 340 nm for a total of 10 minutes.

2.9 F1FO ATP synthase coupling assay.

Enzyme coupling assay was performed by incubating the mitochondria with Oligomycin A at the mentioned concentration for 15 minutes at room temperature before measuring the enzymatic activity of F1FO ATP synthase (Beck et al., 2016).

2.10 Oxygen Consumption Assay.

Oxygen consumption from mitochondria was measured polarographically using a temperature-regulated Clark-type oxygen electrode (Oxytherm, Hansatech). Freshly isolated brain mitochondria were added to the magnetically-stirred chamber and energized with 5 mM Glutamate/Malate (Sigma). To measure the respiration control ratio (RCR), 300 μM ADP was added and state III was measured. Once exogenous ADP is used up, mitochondria enter state IV respiration. RCR was measured as a ratio of state III/state IV. The ADP:O ratio was calculated as the ratio of ADP conversion rate at state III respiration to two fold of oxygen consumption rate at state III respiration (Salin et al., 2016).

2.11 ATP measurement.

ATP synthesis from freshly isolated mitochondria or cultured neurons was measured using a Luminescence ATP detection Assay Kit (Abcam) according to manufacturer's instructions. Luminescence was detected using a microplate reader (synergy Mx., Biotek) controlled by Gen5 software. Standard curve was prepared using ATP as substrate and luminescence readings were expressed in fold change.

2.12 Mitochondrial swelling assay.

Mitochondria swelling was performed on freshly isolated mitochondria. Neuronal mitochondria were suspended in 0.5 mL of swelling assay buffer [50 μg of mitochondrial protein, 150 mM KCl, 5 mM HEPES, 2 mM K_2HPO_4, 5 mM glutamate (pH 7.2)]. Mitochondrial swelling was triggered by the addition of calcium (500 nmol/mg of protein). Swelling was observed by immediately and continuously recording changes in OD values at 540 nm by using a spectrophotometer (Ultrospect 2100, Amersham Biosciences).

2.13 Mitochondrial calcium retention capacity (CRC) assay.

Mitochondrial calcium uptake potential was measured as previously described with Calcium Green™−5N (Invitrogen, Cat# C3737) (Du et al., 2008). Briefly, 40 μg mitochondria suspended in potassium buffer (150 mM KCl, 5 mM Hepes, 2 mM K_2HPO_4, 5 mM Glutamate/Malate, pH 7.2) containing 1 μM Calcium Green™−5N were stimulated with 0.01 μM Calcium strokes every 2 minutes. Ca^{2+} triggered fluorescent signals at 506 nm (excitation) and 532 nm (emission) wavelengths were continuously detected using a microplate reader (BioTek). The emission intensity decreased with mitochondrial calcium uptake. Mitochondrial Calcium Retention Capacity was determined using the total nanomole of Ca^{2+} uptake by per milligram of mitochondria.

2.14 Immunocytochemistry.

Mouse brains were dissected and immediately fixed in 4% paraformaldehyde (PFA) (Sigma-Aldrich) for 24–26 hours at 4 °C. The frozen tissue sections were prepared as previously described (Tian et al., 2019). Primary cultured neurons at DIV14 cultured on Lab-Tek chamber slides were fixed in 4% PFA for 30 minutes at 37 °C. The slices or neurons were blocked with blocking buffer (5% goat or donkey serum, 0.3% Triton X-100 in PBS, pH 7.4) for 1 hour, then incubated with primary antibodies at room temperature overnight. The following primary antibodies were used: mouse anti-PSD95 antibody (Cell Signaling Technology, 36233, 1:400), guinea pig anti-vesicular glutamate transporter 1 (vGlut1, Synaptic Systems, 135304, 1:400), anti-Iba1 (Abcam, ab5076, 1:600), rabbit anti-synaptophysin (Cell Signaling, Technology, 5461, 1:500), and mouse anti-C1q (Abcam, ab71940, 1:300). After washing with PBS, the slices or neurons were then probed with appropriate cross-adsorbed secondary antibodies conjugated to Alexa Fluor 488, Alexa Fluor 594, or Alexa Fluor 647 (Thermo Fisher Scientific, 1:500). Images were collected under a Nikon confocal microscope followed by three-dimensional reconstruction and analysis using Nikon NIS Elements Advanced Research Software. The synapses were defined by colocalization of vGlut1 and PSD95 which was analyzed by using the "AND" operation in the "binary operation" dialog of NIS element software to overlap two binary

layers. The number of synapses was counted and divided by total volume of the image stack. C1q-tagged synapses were defined by colocalization of C1q and synaptophysin and calculated as the ratio of C1q-colocalized synaptophysin to total synaptophysin (volume/volume). Synaptic pruning was examined through co-staining of Iba1 and synaptophysin and calculated as the ratio of engulfed synaptophysin by microglia to total synaptophysin (volume/volume).

2.15 Aβ immunostaining.

PFA-fixed frozen brains were sectioned and used for Aβ staining to determine the levels of plaque deposition. After blocking in PBS containing 5% goat serum and 0.3% Triton X-100, the free-floating brain sections were incubated overnight at room temperature with anti-Aβ (CST, 1:1000). After washing with PBS, the slices were probed with cross-adsorbed secondary antibodies conjugated to Alexa Fluor 488 (Thermo Fisher Scientific, 1:500). Neurons were identified by the staining of NISSL blue (Sigma). Images were collected on a Nikon inverted fluorescence microscope. Nikon NIS Elements Advanced Research Software was used for image analysis. Plaque-occupied area was calculated as a percentage ratio of the area of the plaque to that of the cortex.

2.16 Electrophysiological measurement.

For local field potential experiments (LFPs), mice were anesthetized with isoflurane and decapitated. Brains were rapidly extracted and transverse sections (350 μm) of the hippocampus were cut on a vibratome (VT1200S, Leica) in ice-cold oxygenated (95% O_2, 5% CO_2) low sodium ACSF containing the following: 110 mM choline (Sigma-Aldrich), 25 mM $NaHCO_3$ (Fisher Scientific), 1.25 mM NaH_2PO_4 (Fisher Scientific), 2.5 mM KCl (Sigma-Aldrich), 7 mM $MgCl_2$ (Sigma-Aldrich), 0.5 mM $CaCl_2$ (Sigma-Aldrich), 10 mM dextrose (Fisher Scientific), 1.3 mM L-ascorbic acid (Fisher Scientific), and 2.4 mM sodium pyruvate (Sigma-Aldrich). Slices were incubated for at least 1 hour in normal recording ACSF consisting of: 126 mM NaCl (Fisher Scientific), 25 mM $NaHCO_3$, 1.25 mM NaH_2PO_4, 2.5 mM KCl, 1.3 mM $MgCl_2$, 2 mM $CaCl_2$, 10 mM dextrose, 2.4 mM sodium pyruvate, and 1.3 mM L-ascorbic acid, bubbled with 95% O_2 / 5% CO_2. Slices were allowed to rest for 30 minutes after being transferred to the recording chamber. Recordings of LFPs were performed on an Axon Multiclamp 700B amplifier (Molecular Devices), and data were acquired and analyzed using AxoGraph X (AxoGraph Scientific). A tungsten concentric bipolar microelectrode (World Precision Instruments), and a recording glass electrode (1.5 MΩ) filled with recording ACSF were placed approximately 200 μm apart in the Schaffer collateral-commissural pathway in the CA1 region of the hippocampus. Pulses were delivered in 30 second intervals. Before baseline recordings commenced, input-output curves were taken, using 25–150 μA stimulation currents in 25 μA steps. Three sweeps were sampled at each stimulation intensity and averaged to represent the voltage response at each step. Recordings of baseline responses lasted for at least 40 minutes. Stimulation intensity was set to approximately 40% of the minimum intensity required to evoke the maximum response (based on the input-output curve). The stimulation intensity was kept consistent throughout the duration of the experiment. LTP was induced using a theta burst stimulation (TBS) protocol consisting of 10 bursts (5 pulses at 100Hz) repeated at 5 Hz, delivered two times 30 seconds apart. After LTP induction, LFPs were recorded for an additional 60

minutes. The slope of the EPSP was measured in Axograph and sweeps were averaged in bins of 5 for both the baseline and post LTP induction periods. Changes in LFPs are expressed as percentage change from the averaged baseline values.

2.17 ELISA assay for Aβ measurement.

Aβ amounts in mouse cortical or mitochondria samples were measured by using human Aβ40 and Aβ42 ELISA kits (Thermo Fisher Scientific, KHB3481 for Aβ40 and KHB3441 for Aβ42) following the manufacturer's instructions. Tissues were homogenized thoroughly with cold 5 M guanidine HCl/50 mM Tris HCl. The homogenates were incubated at room temperature for 4 hours. The samples were diluted with cold reaction buffer (Dulbecco's phosphate buffered saline with 5% BSA and 1X protease inhibitor cocktail) and centrifuged at 16,000 ×g for 20 minutes at 4 °C. The supernatants were diluted with standard diluent buffer provided in the kit and quantified by ELISA kits. Aβ amounts were normalized to total protein content in the samples.

2.18 Primary neuron culture.

Primary neurons were cultured from nonTg and OSCP OE pups as previously described (Beck et al., 2016). In brief, brain tissues were dissected from day 0 pups and immediately put in cold Hank's balanced salt solution (HBSS, Sigma-Aldrich), dissociated with 0.05% trypsin (Sigma-Aldrich) at 37 °C for 15 minutes followed by 10–15 times trituration. Cells were then passed through a 40 μm mesh cell strainer (Fisher brand) and centrifuged for 5 minutes at 200 × g. The pellet was gently resuspended in neuron culture medium (Neurobasal A with 2% B27 supplement and 0.5mM L-glutamine, Gibco) and plated on poly-D-lysine (Sigma-Aldrich) coated culture plates (Corning) or chamber slides (Nunc) with an appropriate density (Beck et al., 2016). 10 μM 5-fluoro-2'-deoxyuridine (Sigma-Aldrich) and Uridine (Sigma-Aldrich) was added to the neuron cultures to inhibit non-neuronal cell proliferation. Neurons were cultured to 14 days *in vitro* (DIV) for experiment.

2.19 Aβ42 and scrambled Aβ42 preparation.

The Aβ42 oligomer (GenicBio) was prepared as we previously described (Du et al., 2010). Aβ421–1 peptide (Anaspec) was prepared following the manufacturer's instructions.

2.20 Axonal mitochondrial length and volume measurement.

Neurons were infected by lentivirus-expressing mitochondrial-targeted DsRed (mitoDsRed) at DIV7. At DIV13, the neurons were treated with vehicle, 1 μM Aβ42 oligomer or 1 μM scrambled Aβ for 24 hours, respectively and imaged. A process two to three times longer than other processes stemming from the soma was considered to be an axon as previously described (Du et al., 2010). The images were collected on a Nikon inverted fluorescent microscope with on-stage incubator (37 °C, 5% CO_2), and a fluorescent particle with a clear border was identified as a mitochondrion. The axonal mitochondrial length was analyzed by using Nikon NIS Elements Advanced Research software. For axonal mitochondrial volume measurement, the neurons were fixed with 4% paraformaldehyde (Sigma-Aldrich) for 30min. After blocking in 5% BSA and 0.2% Triton X-100 (Sigma-Aldrich) for 1 hour at room temperature, the neurons were stained with rabbit anti-Microtubule associated protein

2 (MAP2) (Cell Signaling Technology, 8707) to determine dendrites and mouse anti-Tau-1 (Cell Signaling Technology, 4019) to determine axons followed by Alexa Fluor 488 conjugated goat anti-rabbit IgG(H+L) secondary antibody (Thermo Fisher Scientific, R37116) and Alexa Fluor 647 conjugated goat anti-mouse IgG(H+L) highly cross-adsorbed secondary antibody (Thermo Fisher Scientific, A32728), respectively. Images were collected under a Nikon confocal microscope followed by three-dimensional reconstruction and analysis was done using Nikon NIS Elements Advanced Research Software.

2.21 Axonal mitochondria movement recording.

The neurons were cultured on glass bottom microplates (Corning, 4580) and treated using the same method as axonal mitochondrial length and volume measurement. Time-lapse images were captured every 5 seconds for a period of 2 minutes using a Nikon inverted fluorescent microscope with CFI plan fluor 40× oil immersion objective lens and on-stage incubator (37 °C, 5% CO_2). A mitochondrion was considered to be non-mobile if it remained stationary for the entire recording period (H et al., 2010). A movement was counted only if there was a displacement more than the length of the mitochondrion. The direction of movement was determined as stationary, anterograde, or retrograde by comparing the displacement between the initial and final positions relative to the cell body. Mitochondrial movement toward the distal end of an axon was considered to be anterograde, whereas movement toward the proximal end was considered to be retrograde. Kymographs were generated using maximum intensity projections to demonstrate the overall movement traces of mitochondria during the recording period (H et al., 2010).

2.22 Mitochondrial membrane potential assay.

Neurons were incubated with 200 nM TMRM (Sigma-Aldrich) for 30 minutes in an incubator (37 °C, 5% CO_2). Thereafter, the neurons were washed with pre-warmed neuron culture medium followed by another 15-minute incubation. TMRM staining was imaged on a Nikon inverted fluorescent microscope with on-stage incubator (37 °C, 5% CO_2). TMRM intensity was analyzed using Nikon NIS Elements Advanced Research software (Beck et al., 2016).

2.23 Mitochondrial superoxide assay for cultured neurons.

Mitochondrial superoxide was measured as previously described (Beck et al., 2016; Kirkland et al., 2007). Cultured neurons were exposed to 2 μM MitoSox Red (Thermo Fisher Scientific, M36008) and 200 nM MitoTracker green (Thermo Fisher Scientific, M7514) for 45 minutes in an incubator (37 °C, 5% CO_2) followed by washing using pre-warmed neuron culture medium. The live neuron nucleus was identified of Hoechst 33342 (Fisher Scientific) staining at a concentration of 1 μg/ml. The images were collected on a Nikon inverted fluorescent microscope with on-stage incubator (37 °C, 5% CO_2) and analyzed using Nikon NIS Elements Advanced Research software.

2.24 4-hydroxynonenal (4-HNE) staining.

4-HNE was measured by immunostaining using specific antibody against 4-HNE (Lu et al., 2015; Majima et al., 2002). Cultured neurons with the expression of mitoDsRed were fixed

in 4% paraformaldehyde for 30 minutes in an incubator (37 ºC, 5% CO_2). After incubation in blocking buffer (5% goat serum, 0.3% Triton, PBS), the neurons were incubated with rabbit anti-4-HNE (Abcam, ab46545) at 4 °C overnight, followed by incubation with Alexa Fluor 488 conjugated goat anti-rabbit IgG(H+L) (Thermo Fisher Scientific, R37116) for 1 hour at room temperature. The images were collected on a Nikon confocal microscope and analyzed using Nikon NIS Elements Advanced Research Software.

2.25 Behavioral Studies.

To study the spatial learning and reference memory in non-AD and AD mice, the Morris water maze task was performed as previously described (Tian et al., 2019; Vorhees and Williams, 2006). Mice were trained to swim and locate a hidden platform in a water-filled tank for 11 days. After 4 sets of training per day, each set lasting for 30 seconds, mice were subjected to a probe test in which the platform was removed. The goal is to identify the quadrant of the platform and measure the passes at the specified location of the platform. HVS Image 2015 software (HVS Image) was used to track and monitor the behavioral testing of the animals.

2.26 Statistical analysis.

Statistical comparisons were performed using GraphPad Prism 7 software. One-way or two-way ANOVA followed by Bonferroni post hoc analysis, or unpaired two-way Student's *t*-test were applied in data analysis. Pearson's correlation coefficient was used for correlation testing. Numbers of replicates and *P* values are stated in each figure legend. All data were expressed as the mean ± s.e.m. except for the box plots which were shown as minimum, maximum, and medium. Significance was concluded when the *P* value was less than 0.05. Significance is indicated by symbols including * ($P < 0.05$), ** ($P < 0.010$), *** ($P < 0.001$), NS (not significant) denotes $P > 0.05$.

3. RESULTS

3.1 OSCP dysfunction is reduced in Thy-1 OSCP/5xFAD mice.

To restore neuronal OSCP with minimal side effects due to excess protein expression, we selected a line of Thy-1 OSCP mice with moderate (~1.4–1.5 fold) OSCP upregulation in neurons (Fig. 1A&B, Fig. 1A nonTg vs 5xFAD: t = 2.043, df = 20, Fig. 1B nonTg vs 5xFAD: t = 3.049, df = 19) and generated Thy-1 OSCP/5xFAD mice by crossbreeding. To examine the consequences of OSCP overexpression, we measured OSCP expression in cortical mitochondrial fractions via immunoblotting. Brain mitochondria were purified from the neocortex of gender- and age-matched non-transgenic (nonTg), 5xFAD, Thy-1 OSCP, and Thy-1 OSCP/5xFAD mice at 4–5 and 9–10 months old. These age ranges were selected based on our previous observations of OSCP changes, mitochondrial dysfunction, synaptic injury, and cognitive impairment in 5xFAD mice (Beck et al., 2016; Gauba et al., 2019; Wang et al., 2016). Densitometric analysis of the immunoreactive bands showed decreased OSCP expression in 5xFAD mice at both ages, which was reversed by OSCP overexpression (Fig. 1A&B, Fig. 1A Fig. 1A 5xFAD vs Thy1-OSCP/5xFAD: t = 3.495, df = 20, Fig. 1B 5xFAD vs Thy1-OSCP/5xFAD: t = 6.543, df = 19). To determine whether OSCP overexpression affects the expression of other major subunits of F1Fo ATP synthase, we

further examined the expression of α, β, γ, a, b, and c subunits. Immunoblotting data showed no change in the content of these subunits across all four groups of mice at the tested ages (Fig. 1A&B, 5xFAD vs Thy-1 OSCP/5xFAD : 4–5 months old α-subunit: t = 0.1373, df = 17, β-subunit: t = 0.2842, df = 19, γ-subunit: t = 1.102, df = 20, a-subunit: t = 1.321, df = 20, b-subunit: t = 0.1629, df = 19, c-subunit: t = 0.8664, df = 14; 9–10 months old α-subunit: t = 1.167, df = 20, β-subunit: t = 0.3393, df = 20, γ-subunit: t = 6301, df = 9, a-subunit: t = 0.6372, df = 9, b-subunit: t = 0.469, df = 9, c-subunit: t = 0.7357, df = 20). The results confirm selective OSCP vulnerability in AD-relevant pathological settings (Beck et al., 2016; Gauba et al., 2019) and the restoration of OSCP expression in Thy-1 OSCP/5xFAD mice.

OSCP interacts with mitochondrial Aβ (Beck et al., 2016; Gauba et al., 2019). OSCP upregulation may therefore promote the formation of OSCP/Aβ complexes. As expected, further assays for in situ OSCP/Aβ interaction, and by proxy, the positive dots of proximity ligation assays (PLA), showed age-dependent increases in OSCP/Aβ complexation in neocortical neurons in Thy-1 OSCP/5xFAD mice when compared with cells from non-OSCP-modulated 5xFAD littermates (Fig. 1C, 4–5-month-old 5xFAD vs Thy1-OSCP/5xFAD: t = 2.761, df = 8, 9–10-month-old 5xFAD vs Thy1-OSCP/5xFAD: t = 2.716, df = 7). Similar results were seen with neuronal mitochondrial fractions from 9–10-month-old 5xFAD and Thy-1 OSCP/5xFAD mice when using co-immunoprecipitation (co-IP) (Fig. 1D1&2). Further co-IP for OSCP and Aβ complexation using mitochondrial membrane-rich fractions also showed decreased mitochondrial membrane-bound OSCP/Aβ complexes (Fig. 1D1&2, 5xFAD vs Thy1-OSCP/5xFAD mitochondria: t = 2.537, df = 7, 5xFAD vs Thy1-OSCP/5xFAD membrane: t = 2.382, df = 7). Of note, OSCP overexpression did not affect Aβ plaque deposition (Supplementary Fig. 1A&B, 4–5-month-old 5xFAD vs Thy-1 OSCP/5xFAD: t = 0.4816, df = 9; 9–10-month-old 5xFAD vs Thy-1 OSCP/5xFAD: t = 0.07155, df = 9) or concentrations of soluble Aβ1–40 or Aβ1–42 in either cortex homogenates (Supplementary Fig. 2A&B, 4–5-month-old 5xFAD vs Thy-1 OSCP/5xFAD Aβ 1–40: t = 0.1683, df = 10; 4–5-month-old 5xFAD vs Thy-1 OSCP/5xFAD Aβ 1–42: t = 0.1087, df = 10; 9–10-month-old 5xFAD vs Thy-1 OSCP/5xFAD Aβ 1–40: t = 0.07729, df = 9, 9–10-month-old 5xFAD vs Thy-1 OSCP/5xFAD Aβ 1–42: t = 0.0428, df = 9) or mitochondrial fractions (Supplementary Fig. 2C&D, 4–5-month-old 5xFAD vs Thy-1 OSCP/5xFAD Aβ 1–40: t = 0.1373, df = 10; 4–5-month-old 5xFAD vs Thy-1 OSCP/5xFAD Aβ 1–42: t = 0.08775, df = 10; 9–10-month-old 5xFAD vs Thy-1 OSCP/5xFAD Aβ 1–40: t = 0.1805, df = 9, 9–10-month-old 5xFAD vs Thy-1 OSCP/5xFAD Aβ 1–42: t = 0.08571, df = 9) from 5xFAD mice. Because F1Fo ATP synthase is located on the inner mitochondrial membrane, these results seem to suggest decreased Aβ interaction with OSCP that is integrated in F1Fo ATP synthase. Such an effect is, at least in part, due to Aβ neutralization by increased “free” OSCP in the mitochondrial matrix. If so, we would expect to see preserved mitochondrial F1Fo ATP synthase activity and improved mitochondrial function in Thy-1 OSCP/5xFAD mice.

3.2 Mitochondrial function is preserved in Thy-1 OSCP/5xFAD mice.

To determine the protective effect of OSCP overexpression on mitochondrial function, we prepared brain mitochondria from gender- and age-matched nonTg, Thy-1 OSCP, 5xFAD,

and Thy-1 OSCP/5xFAD mice at 4–5 and 9–10 months old and subjected them to assays for F1Fo ATP synthase function. Consistent with our previous observation (Beck et al., 2016; Gauba et al., 2019), mitochondria from 5xFAD mice demonstrated decreased F1Fo ATP synthase activity in an age-dependent manner, which was ameliorated in OSCP-overexpressing 5xFAD mice (Fig. 2A1&2, 4–5-month-old 5xFAD vs Thy1-OSCP/5xFAD: t = 5.202, df = 10, 9–10-month-old 5xFAD vs Thy1-OSCP/5xFAD: t = 2.488, df = 6). Next, we examined F1Fo ATP synthase oligomycin sensitivity to reflect F1Fo complex proton-flow coupling (Beck et al., 2016; Joshi et al., 1997). F1Fo ATP synthase oligomycin sensitivity was protected in 5xFAD mice through OSCP overexpression (Fig. 2B1&2, 4–5-month-old 5xFAD vs Thy1-OSCP/5xFAD: 0 μg/mg t = 4.55^{-008}, df = 11, 0.4 μg/mg t = 1.561, df = 7, 1 μg/mg t = 2.488, df = 7, 100 μg/mg t = 2.835, df = 10; 9–10-month-old 5xFAD vs Thy1-OSCP/5xFAD: 0 μg/mg t = 0, df = 6, 0.4 μg/mg t = 9.223, df = 4, 1 μg/mg t = 4.15, df = 4, 100 μg/mg t = 4.041, df = 4), suggesting that OSCP overexpression prevents F1Fo complex function and integrity in Aβ-enriched environments. Notably, Thy-1 OSCP mice did not demonstrate changes in F1Fo ATP synthase when compared with their nonTg littermates (Fig. 2A&B, Fig. 2A 4–5-month-old nonTg vs Thy-1 OSCP: t = 0.3948, df = 10, 9–10 month old nonTg vs Thy-1 OSCP: t = 0.2527, df = 7; Fig. 2B 4–5-month-old nonTg vs Thy1-OSCP: 0 μg/mg t = 2.631^{-007}, df = 10, 0.4 μg/mg t = 0.2043, df = 5, 1 μg/mg t = 0.1946, df = 6, 100 μg/mg t = 0.2656, df = 6; 9–10-month-old nonTg vs Thy1-OSCP: 0 μg/mg t = 0, df = 7, 0.4 μg/mg t = 0.9321, df = 4, 1 μg/mg t = 0.5365, df = 4, 100 μg/mg t = 0.8502, df = 4). Because OSCP overexpression had no effect on the content of other major F1Fo ATP synthase subunits, this suggests that OSCP upregulation has minimal genotypic effects on baseline levels of F1Fo ATP synthase function.

To determine whether preserving F1Fo ATP synthase function via OSCP restoration benefits mitochondria in 5xFAD mice, we examined mitochondrial function in four groups of mice at 4–5 and 9–10 months old. When compared with their age- and gender-matched nonTg counterparts, 5xFAD mice exhibited an age-dependent decrease in mitochondrial respiration control ratio (RCR) (Fig. 2C1&2, 4–5-month-old nonTg vs 5xFAD: t = 3.502, df = 8, 9–10-month-old nonTg vs 5xFAD: t = 4.436, df = 10) along with lessened ATP production (Fig. 2D1&2, 4–5-month-old nonTg vs 5xFAD: t = 7.772, df = 9, 9–10-month-old nonTg vs 5xFAD: t = 7.815, df = 6) and a decreased ADP:O ratio (Fig. 2E1&2, 4–5-month-old nonTg vs 5xFAD: t = 1.300, df = 10, 9–10-month-old nonTg vs 5xFAD: t = 3.100, df = 10). In contrast, these 5xFAD genotypic changes were ameliorated in Thy-1 OSCP/5xFAD mice (Fig. 2C–E , Fig. 2C1&2, 4–5-month-old 5xFAD vs Thy-1 OSCP/5xFAD: t = 3.270, df = 8, 9–10-month-old 5xFAD vs Thy-1 OSCP/5xFAD: t = 5.555, df = 9; Fig. 2D1&2, 4–5-month-old 5xFAD vs Thy-1 OSCP/5xFAD: t = 2.448, df = 9, 9–10-month-old 5xFAD vs Thy-1 OSCP/5xFAD: t = 6.397, df = 9; Fig. 2E1&2, 4–5-month-old 5xFAD vs Thy-1 OSCP/5xFAD: t = 4.118, df = 9, 9–10-month-old 5xFAD vs Thy-1 OSCP/5xFAD: t = 6.891, df = 6), indicating a strong correlation of OSCP aberrations with Aβ-perturbed mitochondrial bioenergetics. Because F1Fo ATP synthase has been linked to mitochondrial Ca^{2+} regulation (Alavian et al., 2014; Amodeo et al., 2017; Beck et al., 2016; Bonora et al., 2017; Gauba et al., 2019), we next performed mitochondrial swelling assays, and found that OSCP-overexpressing 5xFAD mice showed less mitochondrial swelling in response to Ca^{2+} stimulation (Fig. 2F1&2, 4–5-month-old 5xFAD vs Thy-1 OSCP/5xFAD: t = 2.087, df = 13,

9–10-month-old 5xFAD vs Thy-1 OSCP/5xFAD: t = 4.757, df = 9). In consistency with blunted response to Ca^{2+} stimulation-induced swelling, brain mitochondria from Thy-1 OSCP/5×FAD mice exhibited an increased calcium retention capacity (CRC) (Supplementary Fig. 3A&B, 5xFAD vs Thy-1 OSCP/5xFAD: t = 2.970, df = 11). These results together indicate that OSCP overexpression protects against the Aβ-induced decrease in mitochondrial Ca^{2+} handling capacity. Of note, in addition to mitochondrial Ca^{2+} release via mitochondrial permeability transition, mitochondrial Na^{+}/Ca^{2+} exchanger (mNCX) and mitochondrial uniporter complex (uniplex) are critical machineries for mitochondrial Ca^{2+} regulation (Giorgi et al., 2018). To determine whether OSCP overexpression affects mitochondrial uniplex and mNCX, we further performed immunoblotting assays for the expression levels of sodium-calcium exchanger 1 (NCX1) and the major subunits of mitochondrial uniplex including mitochondrial calcium uniporter (MCU), mitochondrial calcium uniporter regulatory subunit MCUb, mitochondrial calcium uptake 1 (Micu1), mitochondrial calcium uptake 2 (Micu2), and mitochondrial calcium uptake 3 (Micu3) as well as essential MCU regulator (EMRE) (Fan et al., 2020). Densitometry analysis of the immunoreactive bands showed no significant difference in the expression of the tested proteins across all four genotypes of mice (Supplementary Fig. 4A–B, 5xFAD vs Thy-1 OSCP/5xFAD: 4–5-month-old mice MCU t = 1.034, df = 20; Micu1 t = 0.3516, df = 20; Micu2 t = 0.4764, df = 20; Micu3 t = 0.6007, df = 20; Mcub t = 0.5417, df = 20; EMRE t = 2.050, df = 20; Ncx1 t = 0.1759, df = 20; 9–10-month-old MCU t = 1.607, df = 19; Micu1 t = 1.521, df = 20; Micu2 t = 0.8231, df = 20; Micu3 t = 2.007, df = 19; Mcub t = 2.497, df = 17; EMRE t = 0.425, df = 18; Ncx1 t = 0.706, df = 19). These findings, along with preserved F1Fo ATP synthase function, are in line with the detrimental role of F1Fo ATP synthase dysfunction in mitochondrial permeability (Alavian et al., 2014; Amodeo et al., 2017; Beck et al., 2016; Bonora et al., 2017; Gauba et al., 2019). Thy-1 OSCP mice demonstrated similar changes as their nonTg littermates at the tested ages (Fig. 2A–F, Fig. 2A 4–5-month-old nonTg vs Thy-1 OSCP: t = 0.3948, df = 10, 9–10 month old nonTg vs Thy-1 OSCP: t = 0.2527, df = 7; Fig. 2B 4–5-month-old nonTg vs Thy1-OSCP: 0 μg/mg t = 0.3948, df = 10, 0.4 μg/mg t = 0.003173, df = 5, 1 μg/mg t = 0.0658, df = 6, 100 μg/mg t 0.187, df = 6; 9–10-month-old nonTg vs Thy1-OSCP: 0 μg/mg t = 0.253, df = 7, 0.4 μg/mg t = 0.831, df = 4, 1 μg/mg t = 0.5144, df = 4, 100 μg/mg t = 0.9311, df = 4; Fig. 2C 4–5-month-old nonTg vs Thy-1 OSCP: t = 0.8123, df = 9, 9–10-month-old nonTg vs Thy-1 OSCP: t = 1.321, df = 11; Fig. 2D 4–5 month old nonTg vs Thy-1 OSCP: t = 0.3509, df = 9, 9–10-month-old nonTg vs Thy-1 OSCP: t = 1.024, df = 11; Fig. 2E 4–5-month-old nonTg vs Thy-1 OSCP: t = 1.197, df = 10, 9–10-month-old nonTg vs Thy-1 OSCP: t = 0.450, df = 6; Fig. 2F 4–5-month-old nonTg vs Thy-1 OSCP: t = 1.392, df = 8, 9–10-month-old nonTg vs Thy-1 OSCP: t = 0.2355, df = 10. Supplementary Fig. 3, nonTg vs Thy-1 OSCP: t = 1.340, df = 11, Supplementary Fig. 4 nonTg vs Thy-1 OSCP: 4–5-month-old mice MCU t = 0.8044, df = 20; Micu1 t = 0.2883, df = 20; Micu2 t = 0.8195, df = 20; Micu3 t = 0.7132, df = 20; Mcub t = 0.4546, df = 20; EMRE t = 0.3700, df = 20; Ncx1 t = 0.5398, df = 20; 9–10-month-old MCU t = 1.269, df = 19; Micu1 t = 0.3247, df = 20; Micu2 t = 2.733, df = 20; Micu3 t = 1.678, df = 19; Mcub t = 1.831, df = 17; EMRE t = 0.1520, df = 18; Ncx1 t = 0.8390, df = 19), indicating little genotypic effect of OSCP overexpression. Taken together, these results underline the contribution of OSCP dysfunction to mitochondrial deficits in AD-related

pathological settings and they demonstrate that OSCP restoration protects mitochondrial function against Aβ toxicity.

3.3 OSCP modulation protects axonal mitochondrial dynamics and motility against Aβ toxicity.

Neuronal mitochondria are dynamic organelles (Sheng and Cai, 2012; Su et al., 2010). The appropriate size and active transport of axonal mitochondria are pivotal for synaptic physiology (Sheng and Cai, 2012). Defects in axonal mitochondrial dynamics and motility are hallmarks of neuronal mitochondrial pathology in AD, and they reflect mitochondrial functional deficits (Guo et al., 2013; Manczak et al., 2011; Sheng and Cai, 2012; Su et al., 2010). For this reason, we wondered whether OSCP restoration also attenuates the damage to axonal mitochondrial morphology control and mitochondrial trafficking in AD-related conditions. Due to technical difficulties involved in observing axonal mitochondrial movement in vivo, we employed an in vitro system using cultured neurons from nonTg and Thy-1 OSCP pups and exposed them to 500 nM oligomeric Aβ1–42 for 24 hours. Scrambled Aβ1–42 at the same concentration was used as a control to determine the specificity of Aβ toxicity. In order to ensure that the in vitro system recapitulates changes that occur in vivo, we first performed immunoblotting and observed lowered OSCP expression in oligomeric Aβ1–42-treated neurons, which was prevented by OSCP overexpression (Supplementary Fig. 5A&B, vehicle vs Aβ: $t = 0.08461$, $df = 8$, Aβ vs Thy-1 OSCP/Aβ: $t = 2.146$, $df = 8$). In addition to OSCP content, OSCP overexpression rescued mitochondrial bioenergetics from oligomeric Aβ1–42 toxicity as demonstrated by the restoration of mitochondrial membrane potential (mΔΨ) (Supplementary Fig. 6A1&2, Aβ vs OSCP OE/Aβ: $t = 12.21$, $df = 1$) and ATP content (Supplementary Fig. 6B, Aβ vs OSCP OE/Aβ: $t = 4.256$, $df = 1$). Furthermore, compared with their nonTg counterparts, oligomeric Aβ1–42-treated OSCP-overexpressing neurons had decreased mitochondrial MitoSox red intensity (Supplementary Fig. 6C1&2, Aβ vs OSCP OE/Aβ: $t = 9.086$, $df = 8$) along with reduced intra-neuronal (Supplementary Fig. 6D1&3, Aβ vs OSCP OE/Aβ: $t = 4.356$, $df = 8$) and intra-mitochondrial (Supplementary Fig. 6D2&3, Aβ vs OSCP OE/Aβ: $t = 4.91$, $df = 8$) 4-Hydroxynonenal (4-HNE) intensity. These results validate a link between OSCP, mitochondrial defects, and neuronal oxidation due to compromised mitochondrial OXPHOS efficacy in Aβ-rich milieus, and they also indicate that our in vitro system reliably replicates changes that occur in vivo. Next, we used mitoDsRed (Guo et al., 2013) and measured the length of axonal mitochondria to assess axonal mitochondrial dynamics in cultured neurons. OSCP-overexpressing neurons had an average axonal mitochondrial length of 1.62 ± 0.05 μm, which was comparable with that of vehicle-treated nonTg neurons (1.51 ± 0.06 μm, $P>0.05$) (Fig. 3A1&2, vehicle vs OSCP: $t = 0.1888$, $df = 1472$). Furthermore, there was no significant difference in the distribution patterns of axonal mitochondrial length between the two types of neurons (Fig. 3B). The result indicates that OSCP overexpression does not affect baseline axonal mitochondrial length. Oligomeric Aβ1–42 treatment on nonTg neurons induced a significant reduction in the average axonal mitochondrial length (Fig. 3A1&2, vehicle vs Aβ: $t = 5.596$, $df = 1472$), demonstrated by a leftward shift in the cumulative length distribution (Fig. 3B), suggesting increased axonal mitochondrial fragmentation due to oligomeric Aβ1–42 toxicity. Scrambled Aβ1–42 had no effect on mitochondrial length, indicating the specificity of Aβ toxicity (Fig. 3A&B, vehicle vs

scrambled Aβ: t = 1.162, df = 1472). In contrast, OSCP-overexpressing neurons showed increased resistance to oligomeric Aβ1–42-induced axonal mitochondrial fission (Fig. 3A&B, Aβ vs OSCP OE/Aβ: t = 4.99, df = 1472). Because two-dimensional measurements of mitochondrial length may not accurately reflect mitochondrial size we also examined axonal mitochondrial volume. Similar to the measures of axonal mitochondrial length, the oligomeric Aβ1–42 application decreased axonal mitochondrial volume, which was mitigated by OSCP overexpression (Fig. 3C1&2, D, Aβ vs OSCP OE/Aβ: t = 4.825, df = 1438). Mitochondria from 9–10-month-old 5xFAD mice also exhibited elevated phosphorylation of dynamin-like protein 1 (Dlp1) at Ser16 with decreased expression of optic atrophy 1 (Opa1) short (Opa1-S) and long (Opa1-L) isoforms when compared with cells from nonTg controls (Fig. 3E1&2, nonTg vs 5xFAD p-Dlp1^{ser616}: t = 5.956, df = 10; T-Dlp1: t = 0.8314, df = 10; Opa1-S: t = 3.352, df = 10; Opa-L: t = 3.441, df = 10), further suggesting increased mitochondrial fission in oligomeric Aβ1–42-exposed neurons. These 5xFAD genotypic changes in mitochondrial fusion and fission proteins were rescued by OSCP overexpression (Fig. 3E1&2, 5xFAD vs Thy-1 OSCP/5xFAD p-Dlp1^{ser616}: t = 3.965, df = 6; T-Dlp1: t = 1.984, df = 5; Opa1-S: t = 7.846, df = 5; Opa-L: t = 7.169, df = 5). Therefore, we postulate a beneficial effect on mitochondrial dynamics by OSCP overexpression in 5xFAD mice as observed in vitro. Next, we examined axonal mitochondrial trafficking. Oligomeric Aβ1–42-treated neurons had decreased relative numbers of movable mitochondria (Fig. 3G&J, vehicle vs Aβ: t = 2.28, df =27) and increased relative numbers of stationary mitochondria (Fig. 3F&J, vehicle vs Aβ: t = 2.28, df =27) along with reduced anterograde and retrograde movement of mitochondria (Fig. 3H, I, J, Fig. 3H vehicle vs Aβ: t = 2.743, df =28, Fig. 3I vehicle vs Aβ: t = 0.7982, df = 27). These effects of Aβ toxicity on axonal mitochondrial motility correlate with our previous observations (Guo et al., 2013). Vehicle-treated nonTg and OSCP-overexpressing neurons showed no difference in measures of mitochondrial trafficking (Fig. 3F–J, Fig. 3F vehicle vs OSCP OE: t = 0.0282, df = 28; Fig. 3J vehicle vs OSCP OE: t = 0.0282, df = 28; Fig. 3H vehicle vs OSCP OE: t = 0.297, df = 28; Fig. 3I vehicle vs OSCP OE: t = 0.4766, df =28), but OSCP upregulation attenuated oligomeric Aβ1–42-mediated changes in axonal mitochondrial transport (Fig. 3F-J, Fig. 3F Aβ vs OSCP OE/Aβ: t = 2.145, df = 27; Fig. 3J Aβ vs OSCP OE/Aβ: t = 2.145, df = 27; Fig. 3H Aβ vs OSCP OE/Aβ: t = 2.608, df = 28; Fig. 3I Aβ vs OSCP OE/Aβ: t = 1.079, df = 27). These findings support a relationship between OSCP deregulation and impaired axonal mitochondrial morphology and movement control in Aβ-rich milieus.

3.4 Synaptic plasticity is protected in Thy-1 OSCP/5xFAD mice.

In order to determine whether preservation of neuronal mitochondrial function through OSCP modulation reduces synaptic injury in 5xFAD mice, we examined synaptic density in the hippocampal CA1 region, an AD-sensitive brain area (Padurariu et al., 2012), by immunostaining for the vesicular glutamate transporter 1 (vGlut1, to label presynaptic elements) and post synaptic density 95 (PSD95, to label postsynaptic densities) (Beck et al., 2016). NonTg and Thy-1 OSCP mice showed no differences in their synaptic density at 4–5 and 9–10 months (Fig. 4A1&2, 4–5-month-old nonTg vs Thy1-OSCP: t = 0.07596, df = 16; 9–10-month-old nonTg vs Thy1-OSCP: t = 0.09262, df = 16). In contrast, 5xFAD mice showed a large reduction in synaptic elements, which was ameliorated by OSCP

overexpression (Fig. 4A1&2, 4–5-month-old nonTg vs 5xFAD: t = 12, df = 16; 9–10-month-old nonTg vs 5xFAD: t = 7.136, df = 16; 4–5-month-old 5xFAD vs Thy1-OSCP/5xFAD: t = 10.51, df = 16; 9–10-month-old 5xFAD vs Thy1-OSCP/5xFAD: t = 6.616, df = 16). To determine the functional effects of OSCP modulation on synaptic transmission, we next examined long-term potentiation (LTP) in the hippocampal CA3-CA1 pathway (Beck et al., 2016). Hippocampal slices from 4–5 (Fig. 4B1) and 9–10 (Fig. 4B2) month-old 5xFAD mice showed large deficits in theta burst-evoked LTP as measured by the changes in the slope of the field excitatory postsynaptic potential (fEPSP). The decrease in LTP in 5xFAD mice was lessened through OSCP overexpression (Fig. 4B1&2) without affecting baseline input-output relationships of the evoked responses (Supplementary Fig. 7A&B). OSCP overexpression did not affect LTP induction or maintenance in non-Aβ-expressing mice (Fig. 4A&B, Supplementary Fig. 7A&B), indicating that OSCP modulation by itself did not affect synaptic physiology. These findings support a role of OSCP dysfunction in synaptic deficits in 5xFAD mice.

3.5 Synapse elimination by microglia is reduced in Thy-1 OSCP/5xFAD mice.

Recent studies have highlighted synapse elimination through microglial engulfment in AD (Hong et al., 2016; Rajendran and Paolicelli, 2018) and they have implicated mitochondrial mechanism of synapse pruning (Gyorffy et al., 2018; Meng et al., 2015). In view of the protective effect of OSCP modulation on neuronal mitochondrial function in 5xFAD mice, it is possible that OSCP overexpression may suppress synaptic pruning, contributing to preserved synaptic function as seen in Fig. 4A&B. Weak synapses are tagged by the complement system to facilitate microglial engulfment (Presumey et al., 2017) in diseases, including AD (Hong et al., 2016). To examine whether OSCP overexpression alleviates synapse pruning by microglia in 5xFAD mice, we first examined complement component 1q (C1q) tagging of synapses in the hippocampal CA1 region in four groups of mice at 4–5 and 9–10 months old through immunolabeling of C1q and the presynaptic marker synaptophysin. C1q deposition onto synaptophysin-positive synapses was increased in 5xFAD mice as compared with their age- and gender-matched nonTg littermates (Fig. 5A1&2, 4–5-month-old nonTg vs 5xFAD: t = 6.305, df = 16; 9–10-month-old nonTg vs 5xFAD: t = 0.538, df = 16). In Thy-1 OSCP/5xFAD mice these 5xFAD genotypic effects were attenuated (Fig. 5A1&2, 4–5-month-old 5xFAD vs Thy-1 OSCP/5xFAD: t = 6.585, df = 16; 9–10-month-old 5xFAD vs Thy-1 OSCP/5xFAD: t = 8.24, df = 16). Consistent with these immunostaining results we also observed augmented C1q content in purified synaptosomes from 9–10-month-old 5xFAD mice by immunoblotting (Supplementary Fig. 8A1&2, nonTg vs 5xFAD: t = 3.896, df = 8), and these alterations were significantly attenuated in Thy-1 OSCP/5xFAD mice (Supplementary Fig. 8A1&2, 5xFAD vs Thy-1 OSCP/5xFAD: t = 4.905, df = 8). C1q tagging of synapses leads to microglial elimination of the tagged synapses (Hong et al., 2016). Co-staining of synaptophysin and the microglial marker ionized calcium binding adaptor molecule 1 (Iba1) showed increased synaptophysin content in 5xFAD microglia as compared with nonTg mice (Fig. 5B1&2, 4–5-month-old nonTg vs 5xFAD: t = 2.979, df = 16; 9–10-month-old nonTg vs 5xFAD: t = 3.04, df = 16). OSCP overexpression attenuated these changes in 5xFAD mice (Fig. 5B1&2, 4–5-month-old 5xFAD vs Thy-1 OSCP/5xFAD: t = 3.012, df = 16; 9–10-month-old 5xFAD vs Thy-1 OSCP/5xFAD: t = 3.037, df = 16). Therefore, the above results indicate enhanced microglial

engulfment of synapses in AD-related conditions and a protective effect of OSCP overexpression, which may also contribute to preserved synapse density and strength in OSCP-overexpressing 5xFAD mice.

3.6 Spatial learning and memory are improved in Thy-1 OSCP/5xFAD mice.

Because spatial learning and memory are impaired in AD (Adelstein et al., 1992) we examined the influence of OSCP modulation on cognitive functions in the four age- and gender-matched groups of mice at 4–5 and 9–10 months. Consistent with previous studies (Beck et al., 2016; Gauba et al., 2019; Wang et al., 2016), 5xFAD mice showed compromised spatial navigation (Fig. 6A1&A2,) and impaired spatial reference memory (Fig. 6B1&B2, 4–5-month-old nonTg vs 5xFAD: $t = 3.285$, $df = 24$, 9–10-month-old nonTg vs 5xFAD: $t = 3.576$, $df = 24$). Consistent with the idea that OSCP overexpression protects synaptic strength, Thy-1 OSCP/5xFAD showed improved spatial navigation (Fig. 6A1&A2) and spatial reference memory compared with 5xFAD mice (Fig. 6B1&B2, 4–5-month-old nonTg vs 5xFAD: $t = 2.594$, $df = 24$, 9–10-month-old nonTg vs 5xFAD: $t = 3.287$, $df = 24$), indicating a protective effect of OSCP modulation on AD-like cognitive impairments.

4. DISCUSSION

Amyloid beta (Aβ) is a well-documented key mediator of synaptic injury and cognitive impairment in Alzheimer's disease (AD) (Selkoe, 2002); however, approaches targeting Aβ have had limited disease-modifying effects (Honig et al., 2018; Selkoe, 2019). Moreover, the clinical failures of anti-amyloid agents indicate a more complex pathophysiology of AD, which is not likely to be improved through a single therapeutic approach. The mitochondrial cascade hypothesis is based on observations of mitochondrial defects in patients with AD at both brain and systems levels (Swerdlow, 2018), but it is not a repudiation of Aβ's importance in the development of AD. Current findings seem to suggest that Aβ accumulation presents a prelude to mitochondrial deficits, while the latter exaggerates Aβ neurotoxicity. Consistent with the mitochondrial hypothesis, we previously found a loss of OSCP and OSCP/Aβ interaction in AD brains and 5xFAD mice (Beck et al., 2016; Gauba et al., 2019). These changes compromise OSCP's role in maintaining F1Fo complex stability and function in neurons (Beck et al., 2016). Because F1Fo ATP synthase serves an essential function in mitochondrial fitness (Trombetti et al., 2019; Walker, 2013), we hypothesized that OSCP contributes to mitochondrial dysfunction and synaptic injury in AD. To test this idea, we targeted OSCP defects and found that OSCP overexpression preserved F1Fo ATP synthase function, preserving mitochondrial function, and protecting axonal mitochondrial dynamics and motility, resulting in improved synaptic strength and cognition. These findings, together with other studies, support the mitochondrial cascade hypothesis of AD and establish a link between mitochondrial dysfunction and synaptic deficits. Furthermore, the protective effect of OSCP modulation provides a therapeutic avenue against OSCP dysfunction, which could be a candidate target for future gene therapy.

A critical finding of this study is that OSCP overexpression not only restored OSCP expression, but also attenuated the interaction of Aβ with mitochondrial membrane-bound OSCP. The occurrence of augmented Aβ/OSCP complexation in OSCP-overexpressing

5xFAD mitochondria and reduced Aβ binding to mitochondrial membrane-bond OSCP could be interpreted as protection of functional OSCP that integrates into F1Fo ATP synthase. F1Fo ATP synthase is located on the inner mitochondrial membrane (IMM) (Trombetti et al., 2019). The fact that OSCP overexpression had little impact on the expression of other F1Fo ATP synthase subunits suggests that OSCP modulation is not likely to change the components of this enzyme. This suggests that there is abundant "free" OSCP (i.e. non-F1Fo complex-integrated OSCP) in the mitochondrial matrix, which could neutralize Aβ and leave functional OSCP intact. Another possibility is that Aβ-bound OSCP in the F1Fo complex could be replaced by OSCP that is not conjugated to Aβ, as the interaction with Aβ alters OSCP structural conformation and suppresses the connection of OSCP with other subunits (Beck et al., 2016). Further detailed biostructural studies will help to answer this question. Nevertheless, preserved F1Fo ATP synthase function and integrity serves as strong evidence of preserved OSCP function.

The essential role of the mitochondria in supporting synaptic activity has been well documented. The preserved synaptic function in OSCP-overexpressing 5xFAD mice may result from the restoration of mitochondrial energy production, Ca^{2+} modulating capacity, axonal mitochondrial morphology and positioning control, and suppressed mitochondrial oxidative stress. Recent studies have highlighted microglia-mediated synapse elimination in the development of synaptic failure in AD (Hong et al., 2016). Although such a process has been largely attributed to microglial activation in response to Aβ toxicity and resultant neuronal death, emerging evidence suggests a mitochondrial role in synapse pruning and the subsequent synaptoapoptosis (Gyorffy et al., 2018; Meng et al., 2015; Sidlauskaite et al., 2018). We found that C1q deposition onto synapses was drastically reduced in Thy-1 OSCP/5xFAD mice as compared to 5xFAD mice, indicating inhibited complement-dependent synaptic pruning via microglial engulfment in Thy-1 OSCP/5xFAD mice. Because OSCP modulation preserved mitochondrial function in neurons, we thus propose that mitochondrial defects have multiple effects on the development of synaptic deficits in AD-related conditions.

An important factor that influences these changes is the loss of OSCP in AD-like conditions. We have seen reduced OSCP expression in neurons in AD brains, as well as in Aβ-enriched environments such as tissue from 5xFAD mice and oligomeric Aβ-exposed neurons (Beck et al., 2016; Gauba et al., 2019). The association between OSCP downregulation and Aβ toxicity implicates a relevance of OSCP to AD. We have previously shown an age-dependent effect of OSCP deficiency (Gauba et al., 2017). Advancing age is a major risk factor for AD, especially its sporadic form (Guerreiro and Bras, 2015). Indeed, brain aging and AD exhibit commonalities in several aspects such as DNA injury and alterations in histone modifications, brain oxidative stress and Ca^{2+} deregulation, as well as synapse loss and microglia-mediated neuroinflammation (Denver and McClean, 2018; Hof and Morrison, 2004; Swerdlow, 2011; Zhang et al., 2014). However, AD differs from brain aging in the patterns of structural brain changes and cognitive impairment, as well as the severity of brain pathologies, especially in the presence of characteristic AD lesions including Aβ plaques and Tauopathy (Denver and McClean, 2018; Hof and Morrison, 2004; Swerdlow, 2011; Zhang et al., 2014). In this regard, the relationship of brain aging and AD may be reconciled by a model in which the two pathological states share some mechanistic links at the cellular

level, and where the age-dependent development of these changes may serve as a critical cofactor and/or promoter for Aβ toxicity, reinforcing AD phenotypes. This model underscores the importance of exploring age-related factors in the understanding of AD pathogenesis. Mitochondria play an essential role in synaptic physiology and neuronal survival (Lee et al., 2018). The strong correlation of brain energy deficiency, oxidative stress, and Ca^{2+} dysmetabolism with synaptic deficits in both brain aging and AD supports the hypothesis that mitochondrial dysfunction is a common pathway of synaptic failure in the two disease conditions (Muller et al., 2010; Reddy and Beal, 2008; Swerdlow, 2018). Thus, it is possible that OSCP loss is part of a mitochondrial pathway that contributes to the conversion of cognitive aging to dementia, especially in the sporadic form of AD. The deleterious effect of Aβ on OSCP expression also suggests expedited OSCP loss in AD-related conditions, which may contribute to the rapid deterioration of cognitive functions in prodromal AD. In this regard, modulation of OSCP holds promise to modify cognitive aging for the prevention of AD onset in addition to a promising avenue for AD treatment.

Previous studies have already identified a variety of mitochondrial deficits accompanying AD, and thus the specific contribution of OSCP needs to be further clarified. Mitochondrial defects include dampened mitochondrial bioenergetics, deregulated mitochondrial dynamics and motility, increased permeability of the mitochondrial membrane, enhanced oxidative stress, as well as altered mtDNA regulation (Manczak et al., 2006; Wang et al., 2009; Wilkins et al., 2016; Ye et al., 2015). In addition to the direct protection on mitochondrial F1Fo ATP synthase and the resultant attenuated mitochondrial OXPHOS efficacy as well as Ca^{2+} handling in AD-related conditions, it is possible that OSCP modulation protects mitochondria through indirect mechanisms. Several mitochondrial proteins, such as amyloid-binding alcohol dehydrogenase (ABAD) (Lustbader et al., 2004), cyclophilin D (CypD) (Du et al., 2008), and F1Fo ATP synthase α subunit (Schmidt et al., 2008) are targets for Aβ-binding. OSCP overexpression buffers mitochondrial Aβ, which could also reduce the interaction of Aβ with other Aβ-binding proteins, providing protection against Aβ toxicity to multiple mitochondrial functions.

In summary, we have demonstrated protective effects of OSCP overexpression on Aβ-induced mitochondrial defects and synaptic injury in an in vivo setting. However, several questions remain unanswered, such as the mechanistic link that connects OSCP-associated neuronal mitochondrial dysfunction and microglial phagocytosis of synapses, the mechanisms of OSCP-related axonal mitochondrial morphology and transport control, and whether OSCP loss primes the conversion of cognitive aging to dementia. The simplest interpretation of the available data suggests that OSCP restoration is protective for mitochondrial and synaptic deficits in AD-relevant pathological settings, making OSCP a potential target for the treatment of AD.

Supplementary Material

Refer to Web version on PubMed Central for supplementary material.

Acknowledgments

FUNDING

This work was supported by research funding from NIH (R00AG037716, R01AG053588, and R01AG059753), and Alzheimer's Association (AARG-16-442863).

REFERENCES

Adelstein TB, Kesner RP, Strassberg DS, 1992. Spatial recognition and spatial order memory in patients with dementia of the Alzheimer's type. Neuropsychologia 30(1), 59–67. [PubMed: 1738470]

Alavian KN, Beutner G, Lazrove E, Sacchetti S, Park HA, Licznerski P, Li H, Nabili P, Hockensmith K, Graham M, Porter GA Jr., Jonas EA, 2014. An uncoupling channel within the c-subunit ring of the F1FO ATP synthase is the mitochondrial permeability transition pore. Proc Natl Acad Sci U S A 111(29), 10580–10585. [PubMed: 24979777]

Amodeo GF, Solesio ME, Pavlov EV, 2017. From ATP synthase dimers to C-ring conformational changes: unified model of the mitochondrial permeability transition pore. Cell Death Dis 8(12), 1. [PubMed: 29233966]

Beck SJ, Guo L, Phensy A, Tian J, Wang L, Tandon N, Gauba E, Lu L, Pascual JM, Kroener S, Du H, 2016. Deregulation of mitochondrial F1FO-ATP synthase via OSCP in Alzheimer's disease. Nat Commun 7, 11483. [PubMed: 27151236]

Bonora M, Morganti C, Morciano G, Pedriali G, Lebiedzinska-Arciszewska M, Aquila G, Giorgi C, Rizzo P, Campo G, Ferrari R, Kroemer G, Wieckowski MR, Galluzzi L, Pinton P, 2017. Mitochondrial permeability transition involves dissociation of F1FO ATP synthase dimers and C-ring conformation. EMBO Rep 18(7), 1077–1089. [PubMed: 28566520]

Denver P, McClean PL, 2018. Distinguishing normal brain aging from the development of Alzheimer's disease: inflammation, insulin signaling and cognition. Neural Regen Res 13(10), 1719–1730. [PubMed: 30136683]

Du H, Guo L, Fang F, Chen D, Sosunov AA, McKhann GM, Yan Y, Wang C, Zhang H, Molkentin JD, Gunn-Moore FJ, Vonsattel JP, Arancio O, Chen JX, Yan SD, 2008. Cyclophilin D deficiency attenuates mitochondrial and neuronal perturbation and ameliorates learning and memory in Alzheimer's disease. Nat Med 14(10), 1097–1105. [PubMed: 18806802]

Du H, Guo L, Yan S, Sosunov AA, McKhann GM, Yan SS, 2010. Early deficits in synaptic mitochondria in an Alzheimer's disease mouse model. Proc Natl Acad Sci U S A 107(43), 18670–18675. [PubMed: 20937894]

Fan M, Zhang J, Tsai CW, Orlando BJ, Rodriguez M, Xu Y, Liao M, Tsai MF, Feng L, 2020. Structure and mechanism of the mitochondrial Ca(2+) uniporter holocomplex. Nature 582(7810), 129–133. [PubMed: 32494073]

Feng G, Mellor RH, Bernstein M, Keller-Peck C, Nguyen QT, Wallace M, Nerbonne JM, Lichtman JW, Sanes JR, 2000. Imaging neuronal subsets in transgenic mice expressing multiple spectral variants of GFP. Neuron 28(1), 41–51. [PubMed: 11086982]

Gauba E, Chen H, Guo L, Du H, 2019. Cyclophilin D deficiency attenuates mitochondrial F1Fo ATP synthase dysfunction via OSCP in Alzheimer's disease. Neurobiol Dis 121, 138–147. [PubMed: 30266287]

Gauba E, Guo L, Du H, 2017. Cyclophilin D Promotes Brain Mitochondrial F1FO ATP Synthase Dysfunction in Aging Mice. J Alzheimers Dis 55(4), 1351–1362. [PubMed: 27834780]

Giorgi C, Marchi S, Pinton P, 2018. The machineries, regulation and cellular functions of mitochondrial calcium. Nat Rev Mol Cell Biol 19(11), 713–730. [PubMed: 30143745]

Guerreiro R, Bras J, 2015. The age factor in Alzheimer's disease. Genome Med 7, 106. [PubMed: 26482651]

Guo L, Du H, Yan S, Wu X, McKhann GM, Chen JX, Yan SS, 2013. Cyclophilin D deficiency rescues axonal mitochondrial transport in Alzheimer's neurons. PLoS One 8(1), e54914.

Guo L, Tian J, Du H, 2017. Mitochondrial Dysfunction and Synaptic Transmission Failure in Alzheimer's Disease. J Alzheimers Dis 57(4), 1071–1086. [PubMed: 27662318]

Gyorffy BA, Kun J, Torok G, Bulyaki E, Borhegyi Z, Gulyassy P, Kis V, Szocsics P, Micsonai A, Matko J, Drahos L, Juhasz G, Kekesi KA, Kardos J, 2018. Local apoptotic-like mechanisms

underlie complement-mediated synaptic pruning. Proc Natl Acad Sci U S A 115(24), 6303–6308. [PubMed: 29844190]

H D, Guo L, Yan S, Sosunov AA, McKhann GM, Yan SS, 2010. Early deficits in synaptic mitochondria in an Alzheimer's disease mouse model. Proceedings of the National Academy of Sciences of the United States of America 107(43), 18670–18675. [PubMed: 20937894]

Hardy JA, Higgins GA, 1992. Alzheimer's disease: the amyloid cascade hypothesis. Science 256(5054), 184–185. [PubMed: 1566067]

Hof PR, Morrison JH, 2004. The aging brain: morphomolecular senescence of cortical circuits. Trends Neurosci 27(10), 607–613. [PubMed: 15374672]

Hong S, Beja-Glasser VF, Nfonoyim BM, Frouin A, Li S, Ramakrishnan S, Merry KM, Shi Q, Rosenthal A, Barres BA, Lemere CA, Selkoe DJ, Stevens B, 2016. Complement and microglia mediate early synapse loss in Alzheimer mouse models. Science 352(6286), 712–716. [PubMed: 27033548]

Honig LS, Vellas B, Woodward M, Boada M, Bullock R, Borrie M, Hager K, Andreasen N, Scarpini E, Liu-Seifert H, Case M, Dean RA, Hake A, Sundell K, Poole Hoffmann V, Carlson C, Khanna R, Mintun M, DeMattos R, Selzler KJ, Siemers E, 2018. Trial of Solanezumab for Mild Dementia Due to Alzheimer's Disease. N Engl J Med 378(4), 321–330. [PubMed: 29365294]

Joshi S, Cao GJ, Nath C, Shah J, 1997. Oligomycin sensitivity conferring protein (OSCP) of bovine heart mitochondrial ATP synthase: high-affinity OSCP-Fo interactions require a local alpha-helix at the C-terminal end of the subunit. Biochemistry 36(36), 10936–10943. [PubMed: 9283085]

Kirkland RA, Saavedra GM, Franklin JL, 2007. Rapid activation of antioxidant defenses by nerve growth factor suppresses reactive oxygen species during neuronal apoptosis: evidence for a role in cytochrome c redistribution. J Neurosci 27(42), 11315–11326. [PubMed: 17942726]

Lee A, Hirabayashi Y, Kwon SK, Lewis TL Jr., Polleux F, 2018. Emerging roles of mitochondria in synaptic transmission and neurodegeneration. Curr Opin Physiol 3, 82–93. [PubMed: 30320242]

Lu L, Guo L, Gauba E, Tian J, Wang L, Tandon N, Shankar M, Beck SJ, Du Y, Du H, 2015. Transient Cerebral Ischemia Promotes Brain Mitochondrial Dysfunction and Exacerbates Cognitive Impairments in Young 5xFAD Mice. PLoS One 10(12), e0144068.

Lustbader JW, Cirilli M, Lin C, Xu HW, Takuma K, Wang N, Caspersen C, Chen X, Pollak S, Chaney M, Trinchese F, Liu S, Gunn-Moore F, Lue LF, Walker DG, Kuppusamy P, Zewier ZL, Arancio O, Stern D, Yan SS, Wu H, 2004. ABAD directly links Abeta to mitochondrial toxicity in Alzheimer's disease. Science 304(5669), 448–452. [PubMed: 15087549]

Ly CV, Verstreken P, 2006. Mitochondria at the synapse. Neuroscientist 12(4), 291–299. [PubMed: 16840705]

Majima HJ, Nakanishi-Ueda T, Ozawa T, 2002. 4-hydroxy-2-nonenal (4-HNE) staining by anti-HNE antibody. Methods Mol Biol 196, 31–34. [PubMed: 12152210]

Manczak M, Anekonda TS, Henson E, Park BS, Quinn J, Reddy PH, 2006. Mitochondria are a direct site of A beta accumulation in Alzheimer's disease neurons: implications for free radical generation and oxidative damage in disease progression. Hum Mol Genet 15(9), 1437–1449. [PubMed: 16551656]

Manczak M, Calkins MJ, Reddy PH, 2011. Impaired mitochondrial dynamics and abnormal interaction of amyloid beta with mitochondrial protein Drp1 in neurons from patients with Alzheimer's disease: implications for neuronal damage. Hum Mol Genet 20(13), 2495–2509. [PubMed: 21459773]

Meng L, Mulcahy B, Cook SJ, Neubauer M, Wan A, Jin Y, Yan D, 2015. The Cell Death Pathway Regulates Synapse Elimination through Cleavage of Gelsolin in Caenorhabditis elegans Neurons. Cell Rep 11(11), 1737–1748. [PubMed: 26074078]

Mosconi L, Pupi A, De Leon MJ, 2008. Brain glucose hypometabolism and oxidative stress in preclinical Alzheimer's disease. Ann N Y Acad Sci 1147, 180–195. [PubMed: 19076441]

Muller WE, Eckert A, Kurz C, Eckert GP, Leuner K, 2010. Mitochondrial dysfunction: common final pathway in brain aging and Alzheimer's disease--therapeutic aspects. Mol Neurobiol 41(2–3), 159–171. [PubMed: 20461558]

Padurariu M, Ciobica A, Mavroudis I, Fotiou D, Baloyannis S, 2012. Hippocampal neuronal loss in the CA1 and CA3 areas of Alzheimer's disease patients. Psychiatr Danub 24(2), 152–158. [PubMed: 22706413]

Presumey J, Bialas AR, Carroll MC, 2017. Complement System in Neural Synapse Elimination in Development and Disease. Adv Immunol 135, 53–79. [PubMed: 28826529]

Querfurth HW, LaFerla FM, 2010. Alzheimer's disease. N Engl J Med 362(4), 329–344. [PubMed: 20107219]

Rajendran L, Paolicelli RC, 2018. Microglia-Mediated Synapse Loss in Alzheimer's Disease. J Neurosci 38(12), 2911–2919. [PubMed: 29563239]

Reddy PH, 2009. Amyloid beta, mitochondrial structural and functional dynamics in Alzheimer's disease. Exp Neurol 218(2), 286–292. [PubMed: 19358844]

Reddy PH, Beal MF, 2008. Amyloid beta, mitochondrial dysfunction and synaptic damage: implications for cognitive decline in aging and Alzheimer's disease. Trends Mol Med 14(2), 45–53. [PubMed: 18218341]

Reddy PH, Tripathi R, Troung Q, Tirumala K, Reddy TP, Anekonda V, Shirendeb UP, Calkins MJ, Reddy AP, Mao P, Manczak M, 2012. Abnormal mitochondrial dynamics and synaptic degeneration as early events in Alzheimer's disease: implications to mitochondria-targeted antioxidant therapeutics. Biochim Biophys Acta 1822(5), 639–649. [PubMed: 22037588]

Rubinstein JL, Walker JE, Henderson R, 2003. Structure of the mitochondrial ATP synthase by electron cryomicroscopy. EMBO J 22(23), 6182–6192. [PubMed: 14633978]

Salin K, Villasevil EM, Auer SK, Anderson GJ, Selman C, Metcalfe NB, Chinopoulos C, 2016. Simultaneous measurement of mitochondrial respiration and ATP production in tissue homogenates and calculation of effective P/O ratios. Physiol Rep 4(20).

Schmidt C, Lepsverdize E, Chi SL, Das AM, Pizzo SV, Dityatev A, Schachner M, 2008. Amyloid precursor protein and amyloid beta-peptide bind to ATP synthase and regulate its activity at the surface of neural cells. Mol Psychiatry 13(10), 953–969. [PubMed: 17726461]

Selkoe DJ, 2002. Alzheimer's disease is a synaptic failure. Science 298(5594), 789–791. [PubMed: 12399581]

Selkoe DJ, 2019. Alzheimer disease and aducanumab: adjusting our approach. Nat Rev Neurol 15(7), 365–366. [PubMed: 31138932]

Sheng ZH, Cai Q, 2012. Mitochondrial transport in neurons: impact on synaptic homeostasis and neurodegeneration. Nat Rev Neurosci 13(2), 77–93. [PubMed: 22218207]

Sidlauskaite E, Gibson JW, Megson IL, Whitfield PD, Tovmasyan A, Batinic-Haberle I, Murphy MP, Moult PR, Cobley JN, 2018. Mitochondrial ROS cause motor deficits induced by synaptic inactivity: Implications for synapse pruning. Redox Biol 16, 344–351. [PubMed: 29587245]

Su B, Wang X, Zheng L, Perry G, Smith MA, Zhu X, 2010. Abnormal mitochondrial dynamics and neurodegenerative diseases. Biochim Biophys Acta 1802(1), 135–142. [PubMed: 19799998]

Swerdlow RH, 2011. Brain aging, Alzheimer's disease, and mitochondria. Biochim Biophys Acta 1812(12), 1630–1639. [PubMed: 21920438]

Swerdlow RH, 2018. Mitochondria and Mitochondrial Cascades in Alzheimer's Disease. J Alzheimers Dis 62(3), 1403–1416. [PubMed: 29036828]

Swerdlow RH, Burns JM, Khan SM, 2014. The Alzheimer's disease mitochondrial cascade hypothesis: progress and perspectives. Biochim Biophys Acta 1842(8), 1219–1231. [PubMed: 24071439]

Tian J, Guo L, Sui S, Driskill C, Phensy A, Wang Q, Gauba E, Zigman JM, Swerdlow RH, Kroener S, Du H, 2019. Disrupted hippocampal growth hormone secretagogue receptor 1alpha interaction with dopamine receptor D1 plays a role in Alzheimer's disease. Sci Transl Med 11(505).

Trombetti F, Pagliarani A, Ventrella V, Algieri C, Nesci S, 2019. Crucial aminoacids in the FO sector of the F1FO-ATP synthase address H(+) across the inner mitochondrial membrane: molecular implications in mitochondrial dysfunctions. Amino Acids 51(4), 579–587. [PubMed: 30798467]

Vorhees CV, Williams MT, 2006. Morris water maze: procedures for assessing spatial and related forms of learning and memory. Nat Protoc 1(2), 848–858. [PubMed: 17406317]

Walker JE, 1998. ATP Synthesis by Rotary Catalysis (Nobel lecture). Angew Chem Int Ed Engl 37(17), 2308–2319. [PubMed: 29710950]

Walker JE, 2013. The ATP synthase: the understood, the uncertain and the unknown. Biochem Soc Trans 41(1), 1–16. [PubMed: 23356252]

Walker JE, Runswick MJ, Poulter L, 1987. ATP synthase from bovine mitochondria. The characterization and sequence analysis of two membrane-associated sub-units and of the corresponding cDNAs. J Mol Biol 197(1), 89–100. [PubMed: 2890767]

Wang L, Guo L, Lu L, Sun H, Shao M, Beck SJ, Li L, Ramachandran J, Du Y, Du H, 2016. Synaptosomal Mitochondrial Dysfunction in 5xFAD Mouse Model of Alzheimer's Disease. PLoS One 11(3), e0150441.

Wang X, Su B, Lee HG, Li X, Perry G, Smith MA, Zhu X, 2009. Impaired balance of mitochondrial fission and fusion in Alzheimer's disease. J Neurosci 29(28), 9090–9103. [PubMed: 19605646]

Wilkens S, Capaldi RA, 1998. ATP synthase's second stalk comes into focus. Nature 393(6680), 29. [PubMed: 9590688]

Wilkins HM, Koppel SJ, Weidling IW, Roy N, Ryan LN, Stanford JA, Swerdlow RH, 2016. Extracellular Mitochondria and Mitochondrial Components Act as Damage-Associated Molecular Pattern Molecules in the Mouse Brain. J Neuroimmune Pharmacol 11(4), 622–628. [PubMed: 27562848]

Ye X, Sun X, Starovoytov V, Cai Q, 2015. Parkin-mediated mitophagy in mutant hAPP neurons and Alzheimer's disease patient brains. Hum Mol Genet 24(10), 2938–2951. [PubMed: 25678552]

Zhang HY, Chen WX, Jiao Y, Xu Y, Zhang XR, Wu JT, 2014. Selective vulnerability related to aging in large-scale resting brain networks. PLoS One 9(10), e108807.

HIGHLIGHTS:

- OSCP overexpression ameliorates OSCP aberrations in 5xFAD mice.
- OSCP overexpression rescues F1Fo ATP synthase function in 5xFAD mice.
- OSCP overexpression confers mitochondrial resistance to Aβ toxicity.
- OSCP overexpression protects synaptic activity in 5xFAD mice.
- OSCP overexpression improves cognitive function in 5xfAD mice.

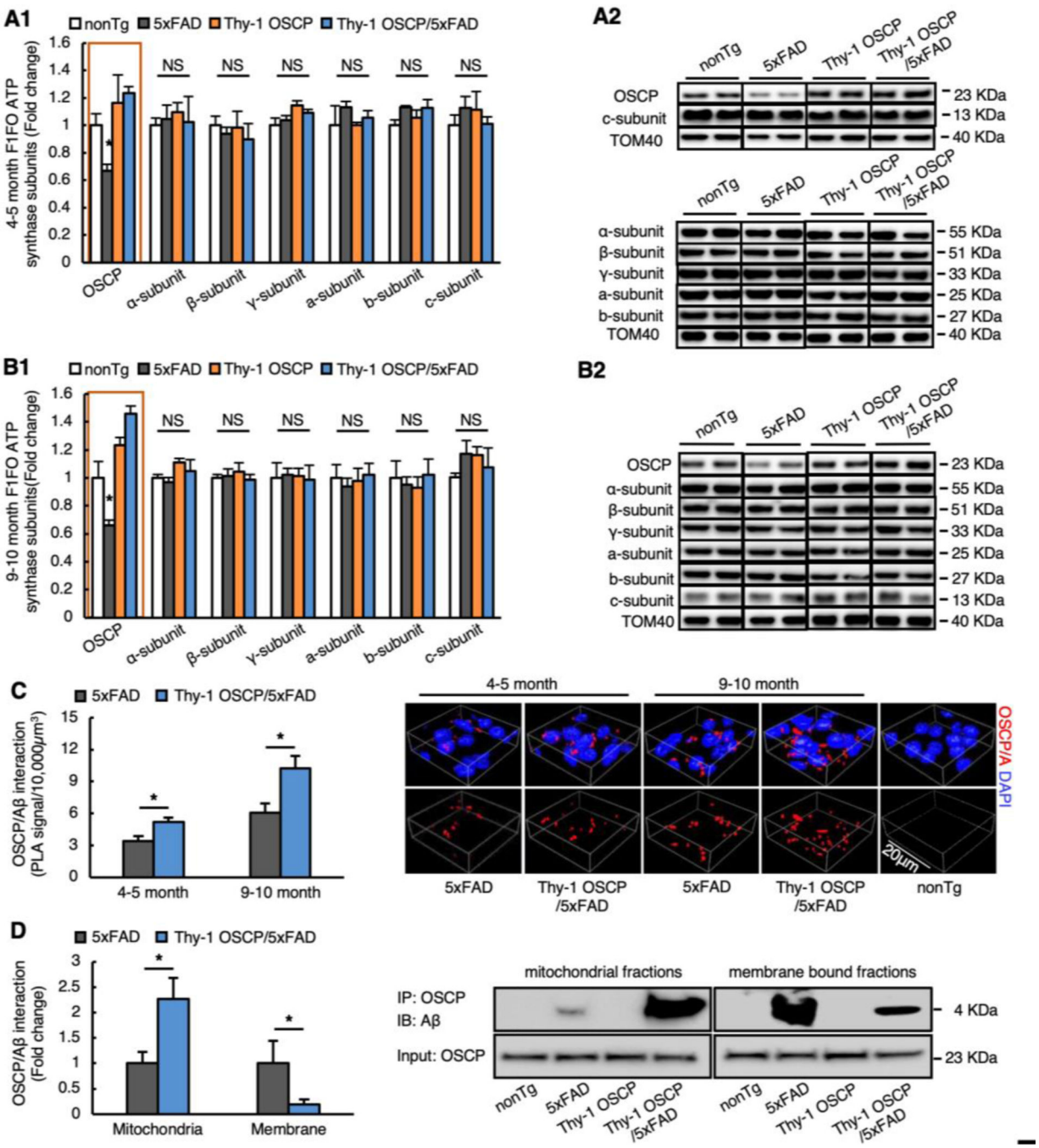

Fig. 1. Alleviated OSCP aberrations in Thy-1 OSCP/5xFAD mice.

(**A&B**) Immunoblotting analysis of OSCP and other major subunits of F1FO ATP synthase including α, β, γ, a, b, and c in brain mitochondria isolated from 4–5 (**A1**) and 9–10-month-old (**B1**) nonTg, 5xFAD, Thy-1 OSCP, and Thy-1 OSCP/5xFAD mice. TOM40 was used as a loading control. Two-way ANOVA followed by Bonferroni post hoc analysis. * $P < 0.05$ 5xFAD vs other groups; NS, not significant. $n = 3–7$ mice per group. (**A2&B2**) Representative bands of immunoblotting. (**C**) Duolink PLA positive dots for OSCP/Aβ complex in cortex from 4–5 and 9–10-month-old 5xFAD and Thy-1 OSCP/5xFAD mice.

Unpaired student *t*-test. * $P < 0.05$. $n = 4–5$ mice per group. The right panel is the 3-dimensional (3D) representative images of OSCP/Aβ PLA positive dots in the cortex. Red dots represent OSCP/Aβ interaction, blue are DAPI-labeled cell nuclei. Scale bar = 20 μm. (**D**) Co-immunoprecipitation (Co-IP) of OSCP and Aβ in isolated mitochondria or their membrane fractions from 9–10-month-old nonTg, 5xFAD, Thy-1 OSCP, and Thy-1 OSCP/5xFAD mice. Right panel are the representative images of Co-IP. Unpaired student *t*-test. * $P < 0.05$. $n = 4–5$ mice per group.

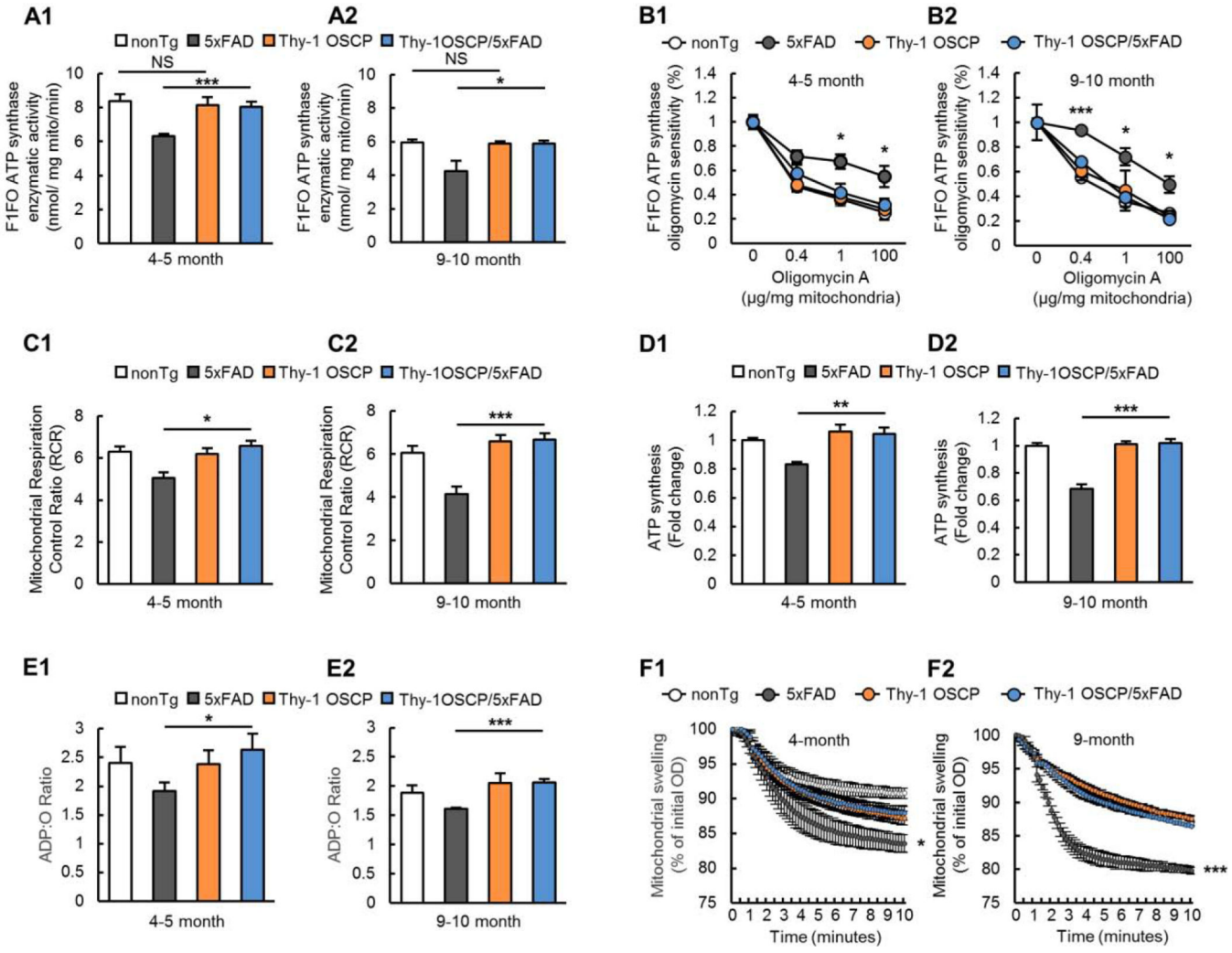

Fig. 2. Attenuated mitochondrial dysfunction in Thy-1 OSCP/5xFAD mice.

(**A**) F1FO ATP synthase catalytic activity of brain mitochondria isolated from 4–5 (**A1**) and 9–10-month-old (**A2**) nonTg, 5xFAD, Thy-1 OSCP, and Thy-1 OSCP/5xFAD mice. Unpaired student *t*-test. * $P < 0.05$, *** $P < 0.001$; NS, not significant. $n = 4–7$ mice per group. (**B**) Oligomycin sensitivity of isolated brain mitochondria from 4–5 (**B1**) and 9–10-month-old (**B2**) nonTg, 5xFAD, Thy-1 OSCP, and Thy-1 OSCP/5xFAD mice. Unpaired student *t*-test. * $P < 0.05$ 5xFAD vs Thy1-OSCP/5xFAD, *** $P < 0.001$ 5xFAD vs Thy1-OSCP/5xFAD. $n = 3–7$ mice per group. (**C**) Mitochondrial respiration control ratio in 4–5 (**C1**) and 9–10-month-old (**C2**) old nonTg, 5xFAD, Thy-1 OSCP, and Thy-1 OSCP/5xFAD mice. Unpaired student *t*-test. * $P < 0.05$, *** $P < 0.001$. $n = 5–7$ mice per group. (**D**) ATP production in isolated brain mitochondria from 4–5 (**D1**) and 9–10-month (**D2**) nonTg, 5xFAD, Thy-1 OSCP, and Thy-1 OSCP/5xFAD mice. Unpaired student *t*-test. ** $P < 0.01$, *** $P < 0.001$. $n = 4–6$ mice per group. (**E**) Mitochondrial ATP:O ratio in 4–5 (**E1**) and 9–10-month-old (**E2**) nonTg, 5xFAD, Thy-1 OSCP and Thy-1 OSCP/5xFAD mice. Unpaired student *t*-test. * $P < 0.05$ vs other groups, *** $P < 0.001$. $n = 4–6$ mice per group. (**F**) Mitochondrial swelling for 4–5 (**F1**) and 9–10-month-old (**F2**) nonTg, 5xFAD, Thy-1 OSCP,

and Thy-1 OSCP/5xFAD mice. Unpaired student *t*-test. * $P < 0.05$ 5xFAD vs Thy1-OSCP/5xFAD, *** $P < 0.001$ 5xFAD vs Thy1-OSCP/5xFAD. $n = 5–9$ mice per group.

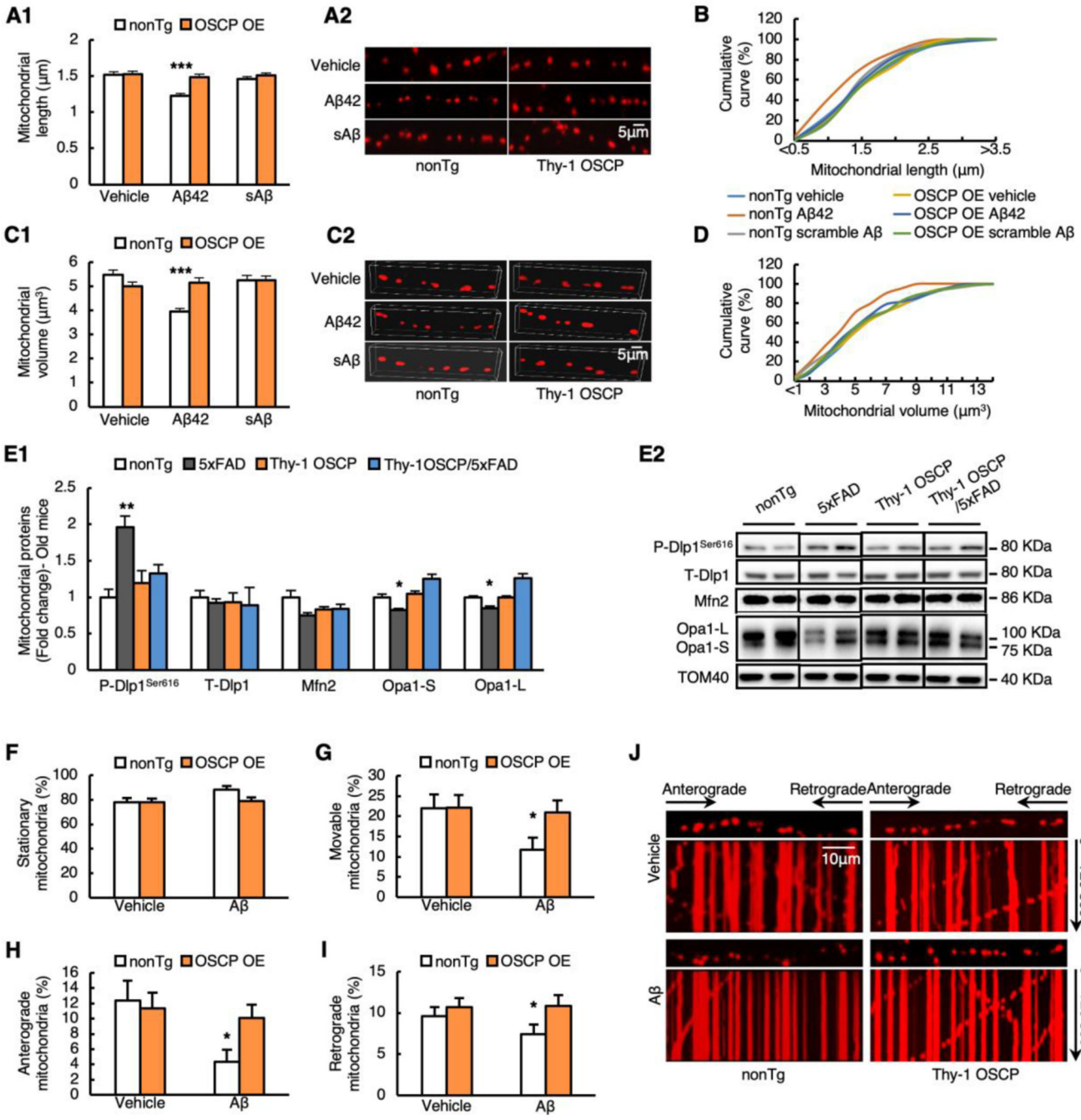

Fig. 3. Rescued axonal mitochondrial dynamic and motility by OSCP overexpression in Aβ-treated neurons.

(**A1**) The average length of axonal mitochondria was measured in primary nonTg and Thy1-OSCP neurons expressing mitoDsred. The neurons were treated with vehicle, 1 μM Aβ1–42, or 1 μM scramble Aβ for 24 hours. Two-way ANOVA followed by Bonferroni post hoc analysis. *** $P < 0.001$. $n = 227–256$ mitochondria per group. (**A2**) Representative images of axonal mitochondria in primary cultured neurons. Scale bar = 5 μm. (**B**) Cumulative distribution data of axonal mitochondrial length. $n = 227–256$ mitochondria per group. (**C1**)

The average volume of axonal mitochondria was analyzed from nonTg and Thy1-OSCP neurons treated with vehicle, 1 μM Aβ1–42 or 1 μM scramble Aβ for 24 hours. Two-way ANOVA followed by Bonferroni post hoc analysis. *** $P < 0.001$. $n = 223–256$ mitochondria per group. (**C2**) Representative 3D images of axonal mitochondria in primary cultured neurons. Scale bar = 5 μm. (**D**) Cumulative distribution data of axonal mitochondrial volume. $n = 223–256$ mitochondria per group. (**E1**) Immunoblotting analysis of mitochondrial dynamic protein in isolated brain mitochondria from 9–10-month-old nonTg, 5xFAD, Thy-1 OSCP, and Thy-1 OSCP/5xFAD mice. p-Dlp1^{Ser616}, T-Dlp1, Mfn2, and OPA1 including short form (OPA1-S) and long form (OPA1-L) were detected. Two-way ANOVA followed by Bonferroni post hoc analysis. * $P < 0.05$ vs other groups. ** $P < 0.01$ vs other groups. $n = 3–4$ mice per group. (**E2**) Representative bands of immunoblotting in E1. (**F-J**) Axonal mitochondrial trafficking including percentage of stationary axonal mitochondria (**F**), percentages of movable (**G**), anterograding (**H**), and retrograding (**I**) mitochondria for vehicle and 24 hours 1 μM Aβ1–42 or 1 μM scramble Aβ-treated nonTg and Thy1-OSCP neurons. Unpaired student *t*-test. * $P < 0.05$ vs other groups. (**J**) Representative kymographs of axonal mitochondrial movement. Scale bar = 10 μm. Data were collected from 3 independent experiments.

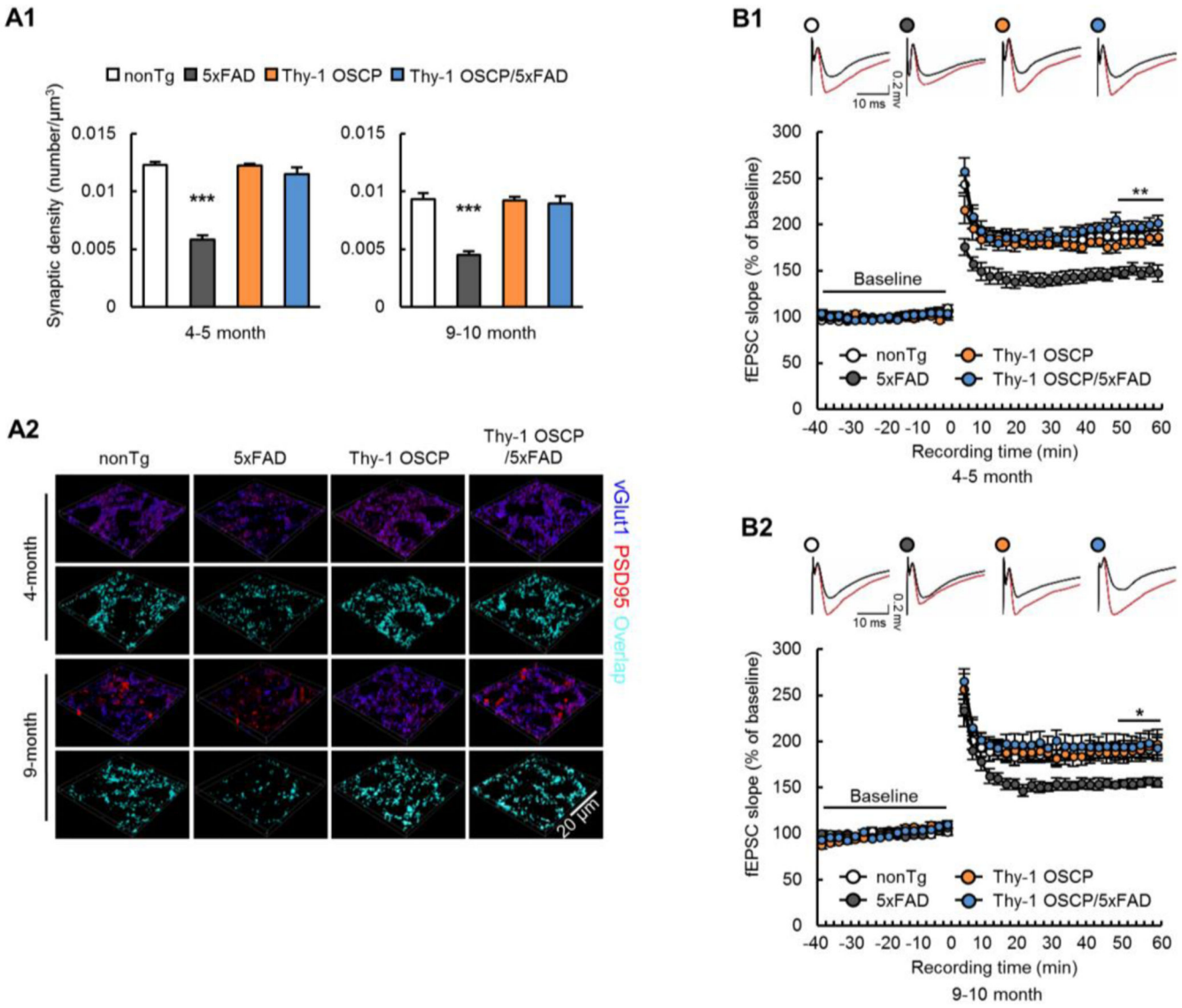

Fig. 4. Preserved synaptic plasticity and transmission in Thy-1 OSCP/5xFAD mice.

(**A1**) Synaptic density of 4–5-and 9–10-month-old nonTg, 5xFAD, Thy-1 OSCP, and Thy-1 OSCP/5xFAD mice. Two-way ANOVA followed by Bonferroni post hoc analysis. *** $P <$ 0.001 vs other groups. $n = 5$ mice per group. (**A2**) Representative 3D-reconstructed images of synapse staining. vGLUT1 (blue) and PSD95 (red) were used to visualize pre- and post-synaptic components, respectively. The overlaid staining of vGLUT1 and PSD95 indicates synapses. Scale bar = 20 µm. (**B**) Time course of long-term-potential (LTP) and representative fEPSP responses during the baseline period (black trace) and 30 seconds after theta burst stimulation (red trace) in four groups of mice at 4–5 (**B1**) and 9–10 (**B2**) months old. Two-way ANOVA followed by Bonferroni post hoc analysis. * $P < 0.05$ 5xFAD vs other groups. ** $P < 0.01$ 5xFAD vs other groups. $n = 6$–9 mice per group.

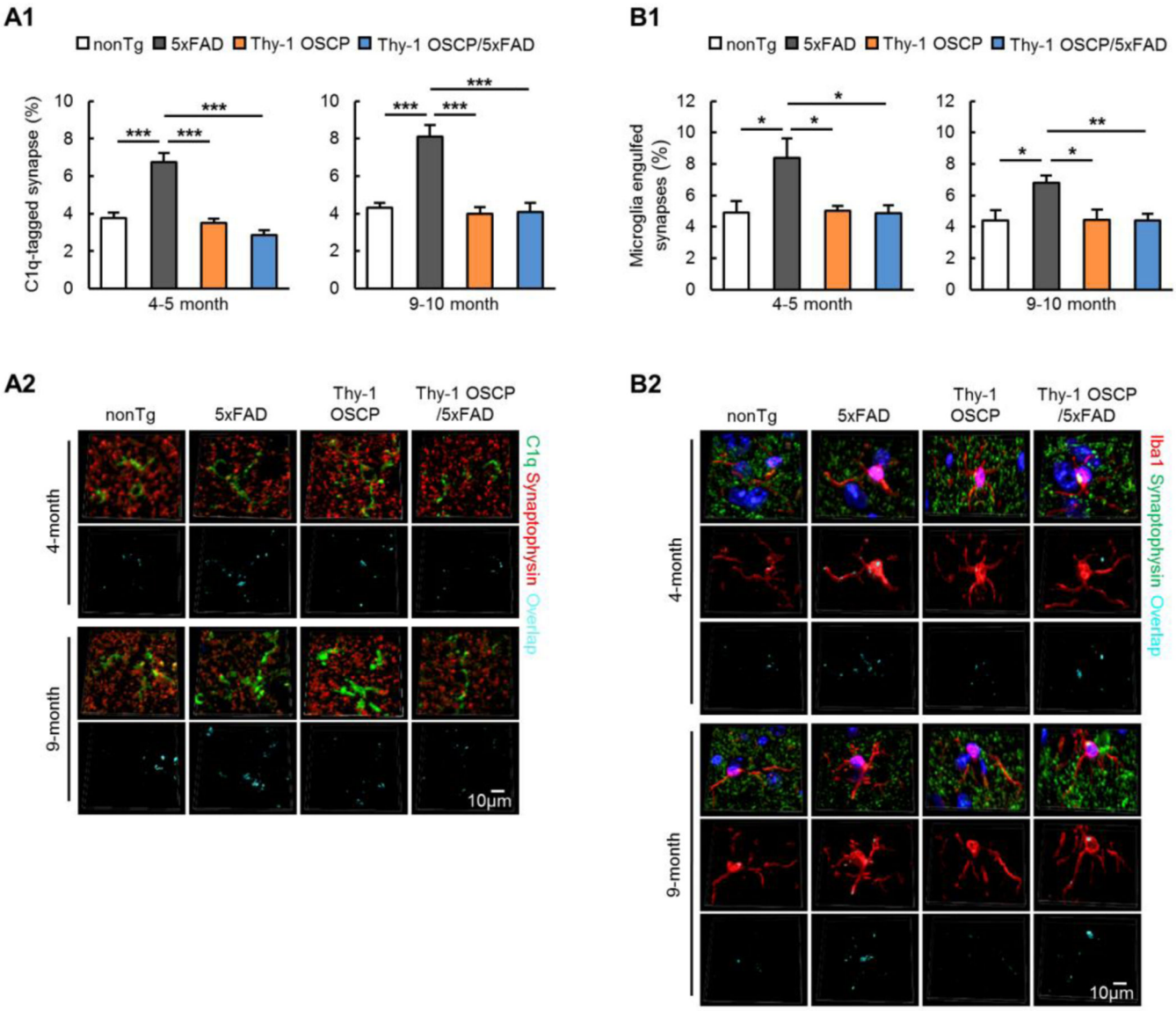

Fig. 5. Mitigated synapse trimming by microglia in Thy-1 OSCP/5xFAD mice.

(**A1**) Analysis of C1q-tagged synapses in cortex from 4–5 and 9–10-month-old nonTg, 5xFAD, Thy-1 OSCP, and Thy-1 OSCP/5xFAD mice. Two-way ANOVA followed by Bonferroni post hoc analysis. *** $P < 0.001$. $n = 5$ mice per group. (**A2**) Representative 3D-reconstructed images of C1q-tagged synapses in cortex. Synaptophysin (red) represents synapses. The overlaid staining of C1q and synaptophysin indicates C1q-tagged synapses. Scale bar = 10 μm. (**B1**) Synaptic pruning was examined through co-staining of microglia (Iba1, red) and synapses (synaptophysin, green). Two-way ANOVA followed by Bonferroni post hoc analysis. * $P < 0.05$, ** $P < 0.01$. $n = 5$ mice per group. (**B2**) 3D representative images of synaptic pruning by microglia. The overlaid staining of Iba1 and synaptophysin indicates microglia-engulfed synapses. Scale bar = 5 μm.

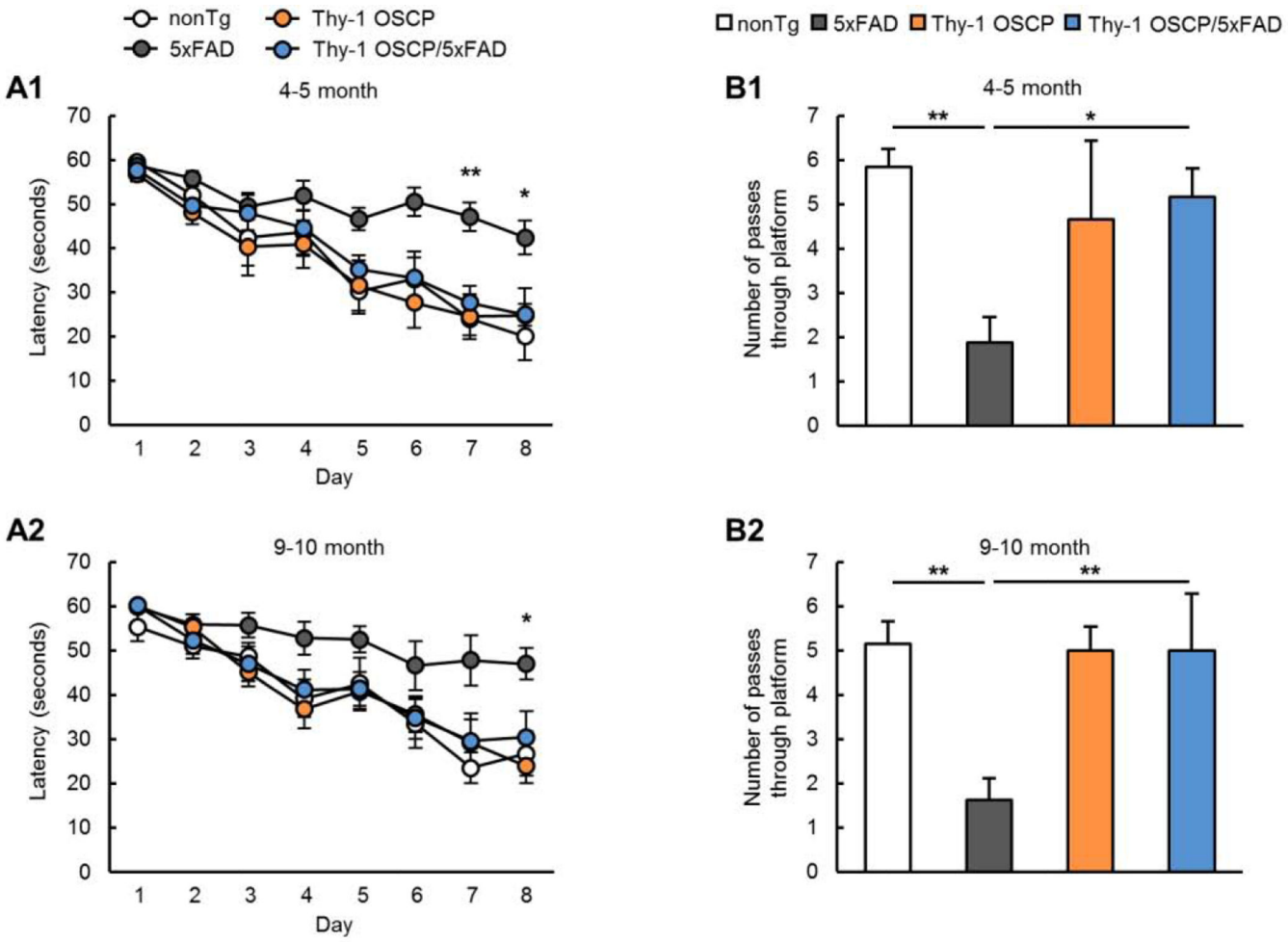

Figure 6. Improved cognitive function in Thy-1 OSCP/5xFAD mice.

Spatial learning (**A1&A2**) and reference memory (**B1&B2**) of 4–5 and 9–10-month-old nonTg, 5xFAD, Thy-1 OSCP, and Thy-1 OSCP/5xFAD mice. One-way ANOVA followed by Bonferroni post hoc analysis. * $P < 0.05$ vs other groups, ** $P < 0.01$ vs other groups. $n =$ 6–9 mice per group.